Spring 5-31-1994

Programmable microstrip dipole antenna design

Jing Zhu
New Jersey Institute of Technology

ABSTRACT

PROGRAMMABLE MICROSTRIP DIPOLE ANTENNA DESIGN

by
Jing Zhu

The narrow bandwidth of microstrip dipole antennas is a major limitation for many applications. A method to increase the microstrip dipole antenna bandwidth is illustrated in this thesis. The proposed method utilizes micromechanical actuators to adjust the electrical length of the dipole antenna. The length change is realized by the activities of several microactuators arranged on both arms of the antenna. The radiation pattern and input impedance, as well as the microactuator mechanisms are detailed in this thesis. A programmable microstrip dipole antenna including the microactuators has been designed with the feedline taken into consideration. The fabrication techniques for this family of programmable antennas are also described.

PROGRAMMABLE MICROSTRIP DIPOLE ANTENNA DESIGN

by
Jing Zhu

A Thesis
Submitted to the Faculty of
New Jersey Institute of Technology
in Partial Fulfillment of the Requirements for the Degree of
Master of Science in Electrical Engineering

Department of Electrical and Computer Engineering

May 1994

APPROVAL PAGE

PROGRAMMABLE MICROSTRIP DIPOLE ANTENNA DESIGN

Jing Zhu

Dr. William N. Carr, Thesis Advisor — Date
Professor and Holder of Sponsored Chair in Microelectronics, NJIT

Dr. Shih-Chang Wu, Thesis Coadvisor — Date
Assistant Professor of Electrical and Computer Engineering, NJIT

Dr. Edip Niver, Committee Member — Date
Professor of Electrical and Computer Engineering, NJIT

BIOGRAPHICAL SKETCH

Author: Jing Zhu

Degree: Master of Science in Electrical Engineering

Date: May, 1994

Undergraduate and Graduate Education:

- Master of Science in Electrical Engineering,
  New Jersey Institute of Technology, Newark, NJ, 1994

- Bachelor of Science in Electrical Engineering
  Shanghai Jiao Tong University, Shanghai, P.R.China, 1987

Major: Electrical Engineering

Presentations and Publications:

J. Zhu and R.H. Jin, "Resonant Frequencies of Electrically Thick Microstrip Antenna," 2nd International Symposium on Antenna and EM Theory, Shanghai, Oct. 1989

This thesis is dedicated to
my parents and my husband

ACKNOWLEDGMENT

The author wishes to express her sincere gratitude to her thesis advisor, Dr. William N. Carr, and coadvisor Dr. Shih-Chang Wu, for their continued support through out this research. Special thanks to Professor Edip Niver for serving on my committee.

The author has been using I_NAC_3 antenna simulator and SMAD(Shaped Microstrip Antennas: Dipoles) simulator for the thesis. Therefore thanks to Compact Software, Inc., Paterson, NJ, and Phraxos Research & Development Inc., Santa Monica, CA, for providing the software, respectively. The author thanks Dr. Xiaoyi Gu and Haimin Yu for their helpful discussions of microactuators during the design phase.

The author would also like to express her appreciation to her friends in NJIT, who have given her kindly assistance. Especially she thanks Ping Wang, Chao Ye, Guan Yang, Chao Sun, Chinhghong Wu, Robert Okojie and Yang Gao for their help.

TABLE OF CONTENTS

Chapter **Page**

LIST OF TABLES

LIST OF FIGURES

Figure **Page**

CHAPTER 1

INTRODUCTION

1.1 Introduction

Printed circuit antennas find increasing use in microwave frequencies as well as in the far infrared. They are ideally suited in those applications where conformal thin antennas are required. They may be used in spacecraft, missiles and high-velocity aircrafts. These antennas can be fabricated to the highest degree of precision because of the development of standard photolithographics techniques.

There are advantages of such kind of antennas. The antennas are flat , have small dimensions and low cost, and are easy to be installed and reproduced. But there are disadvantages which are the low radiation efficiency and narrow bandwidth.

Extensive research has been done on printed antennas recently. The radiation efficiency is not a problem because antenna arrays can be used to get specified gain. The main limitation is the narrow bandwidth.

In this thesis, an innovative model of antenna: programmable microstrip dipole antenna (or programmable printed dipole antenna) is presented. These antennas can have several times wider operating bandwidth than that of conventional ones. The structure of a programmable microstrip antenna differs from that of a conventional one in that: micro electro switches are fabricated on the antenna arms symmetrically. They are controlled to change the length of the antenna to keep the antenna resonant. So the programmable antennas can work in a wider range of frequencies than the conventional antennas.

This thesis is organized as follows: the objective of the thesis, previous works, the basic concepts of a programmable antenna, and overall design is presented in Chapter 1. The operating principles of programmable microstrip dipole antennas are described in Chapter 2. The design technologies of programmable microstrip dipole antenna are

presented in Chapter 3. The mechanism and design of thermal microactuators for the programmable dipole antenna are presented in chapter 4. Chapter 5 is concentrated on the fabrication sequence of the programmable microstrip dipole antennas. The merits of presented investigation as well as the future work with the programmable antenna are summarized in Chapter 6.

1.2 Previous Work on Microactuators

Because of the rapid advances made by silicon IC technology, microelectronic devices and components are used in many new areas and applications. The use of silicon as a mechanical material has led to the development of integrated devices combining transducer elements and microelectronics circuits. So far a variety of micromachined silicon sensors, partially with integrated electronic circuits, has been developed. However no applications on antennas has been reported.

Researches on the microactuator fabrication have been done by many investigators. Various methods have been employed to actuate the devices. The mechanism of thermal effects are discussed [1][2][3][4]. The fabrication of this kind of devices are also reported [5][6][7][8]. Most movable devices are designed to be at rest in one stable position except when a driving force is applied. A few actuators with bistable states [9][5] are also reported.

1.3 Basic Concepts of Programmable Antennas

The input impedance of antenna is one of the key parameter to govern the antenna bandwidth characteristics. The imaginary part of the input impedance is always preferred to be zero to get resonance. Input impedance is sensitive to frequencies. The bandwidth of the antenna, especially microstrip antenna, is a major problem.

Actually the input impedance is corresponded with the current distribution on both arms of the antenna. This current distribution is a function of the dipole length. It is

possible to change the length of dipole so that the input impedance is almost fixed in a wide range of working frequencies. The major work in this thesis is to design the length changeable antenna, which is called the programmable antenna.

A diagram of a programmable dipole antenna is shown in Figure 1.1. This programmable antenna is very similar to a fixed-length dipole except that the programmable antenna has micro electro switches on both arms. These switches are symmetrically arranged at certain positions. These switches are realized by microactuators which can be turned to either enabled or disabled. The symmetrical pair is always the same mode. External forces such as thermal, magnetic field, etc., can be used to turn on the switches. Thermally excited microactuators are used in this design.

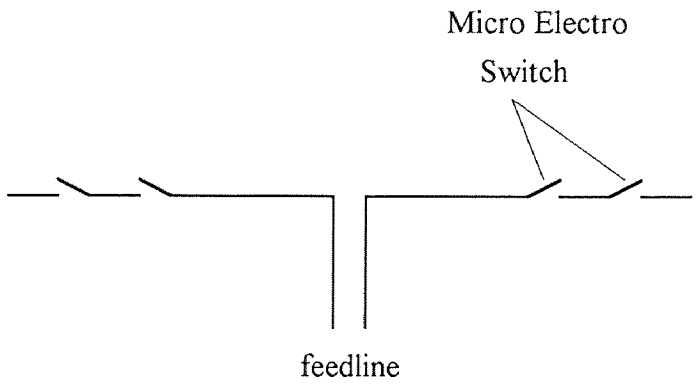

Figure 1.1 Diagram of programmable dipole antenna

When a switch is off(open circuit), the antenna arm is disconnected and becomes shorter. When a switch is on(short circuit), the antenna arm is extended and becomes longer. The radiation pattern is not significantly affected but the input impedance changes when the microactuators turn on or turn off. This antenna can be tuned to adapt the

working frequency using the microactuators. Therefore the bandwidth of printed antennas can be enhanced for multiband, sequential-tuning applications.

1.4 Overall Design

A programmable microstrip antenna system consists of input circuit, antenna, and control circuit. A top view of this antenna system is shown in Figure 1.2. These schematics are not to scale. The input circuit is fabricated on chip 2 and it contains the transmission line and a balun. The antenna with microactuators are fabricated on chip 1. Chip 1 has both top and bottom ground plane. Chip 2 and chip 1 are connected through interchip bonding. Signals are input to antenna by this interconnection. The dashed lines on chip 1 are the transmission line to send the control signals to mciroactuators. These transmission lines are covered by the top ground plane. This will prevent the transmission lines from affecting the antenna radiation pattern.

The design of the programmable antenna on chip 1 is focused. This design includes the antenna design, actuator position choosing, and Microactuator design.

During the microactuator design both the beam deflection and the heater resistance must be considered carefully. The deflections and forces for a good contact between antenna and microactuators are crucial and will be discussed. The n^+-poly beam layer is not only the actuation element but also the heating element. The power needed for the heater will be also estimated.

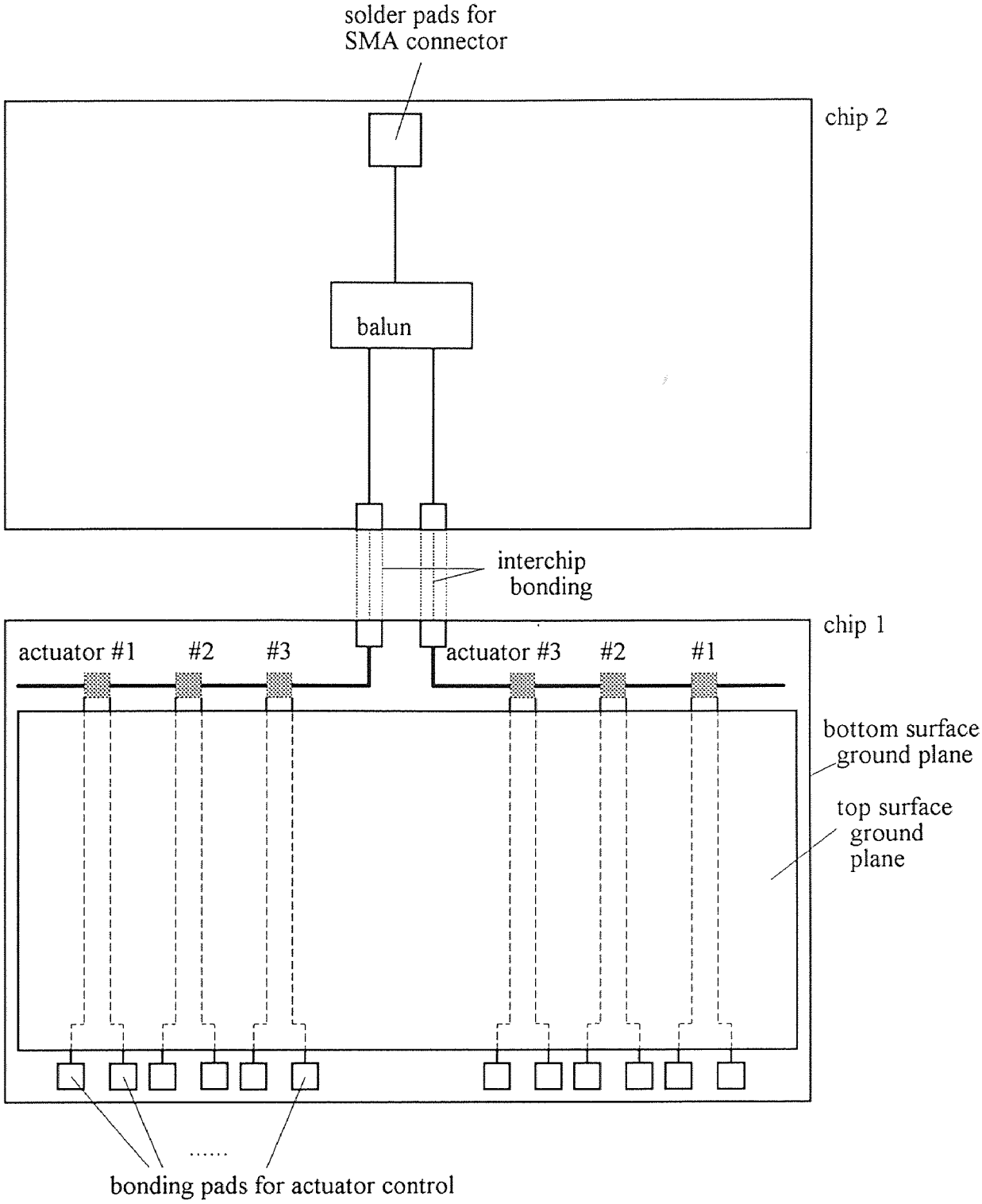

Figure 1.2 Top view of overall design for programmable antenna system (not to scale)

CHAPTER 2

PRINCIPLES OF OPERATION

2.1 Input Impedance of Dipole Antenna

Dipole is one of the most common radiators. It is a straight conductor (often a thin wire or circular cylinder) broken at some point where it is excited by a voltage derived from a transmission line , waveguide, or directly from a generator . Figure 2.1 shows a typical dipole antenna with a center-driven introduced by transmission line. This antenna is with total length $2l$. The half-wave dipole with the length $2l$ approximately equal to a half-wavelength is very common and finds widespread use in thousands of applications.

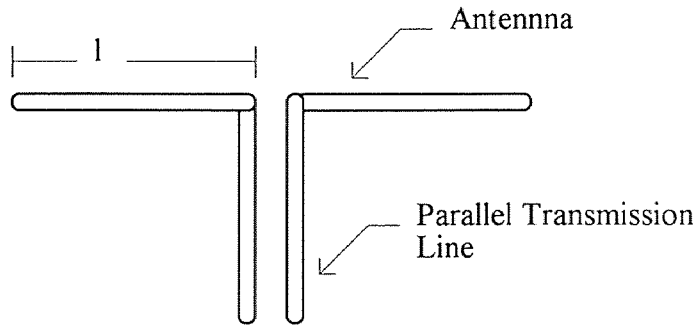

Figure 2.1 A typical dipole antenna with parallel transmission line

The input impedance characteristics of cylindrical antennas have been investigated by many researchers. Theoretical work has mainly been confined to relatively thin antennas (length-to-diameter ratio greater than 15), and the effect of the junction connecting the antenna proper and the transmission line is usually not considered. Among

various theories, the induced-emf method of computing the impedance of a cylindrical antenna based upon a sinusoidal distribution has been widely used. The formula derived from this method is extremely simple. It is, however, valid only when the half length of a center-driven antenna is not much longer than a quarter wavelength. In practice this is the most useful range. The antennas described here are also in this range. The input impedance of the center-driven antenna is in following form [10]:

$$Z_i = R(kl) - j[120(\ln\frac{l}{a} - 1)\cot kl - X(kl)] \tag{2.1}$$

where Z_i = input impedance, Ω, of a center-driven cylindrical antenna of total length $2l$ and radius a

$kl = 2\pi(l/\lambda)$ = electrical length , corresponding to l, measured in radius

$R(kl)$ and $X(kl)$ can be found in Reference[10]

It is shown in (2.1) that the input impedance is a function of the antenna length and frequency. The wavelength and resonant frequency has the following relationship

$$f_o = c/\lambda \tag{2.2}$$

where c is the speed of light.

2.2 Resonant Frequency Control

It is mentioned in Chapter 1 that the microactuators in Figure 1.1 can be switched to change the length of the antenna. A more detailed model is shown in Figure 2.2. The center-driven dipole antenna is 1mm above the infinite ground surface. The labeled movable plates above the discontinuities on the antenna arms are thermal microactuators.

These microactuators can be moved up and down controlled by thermal energy. There are total 6 pairs of thermal actuators(microelectromechanical switches) which are labeled from #1 to #6 in Figure 2.2. The thermal microactuators will be discussed in detail in the next chapters. The antenna model in Figure 2.2 is a simple model for programmable microstrip dipole antenna.

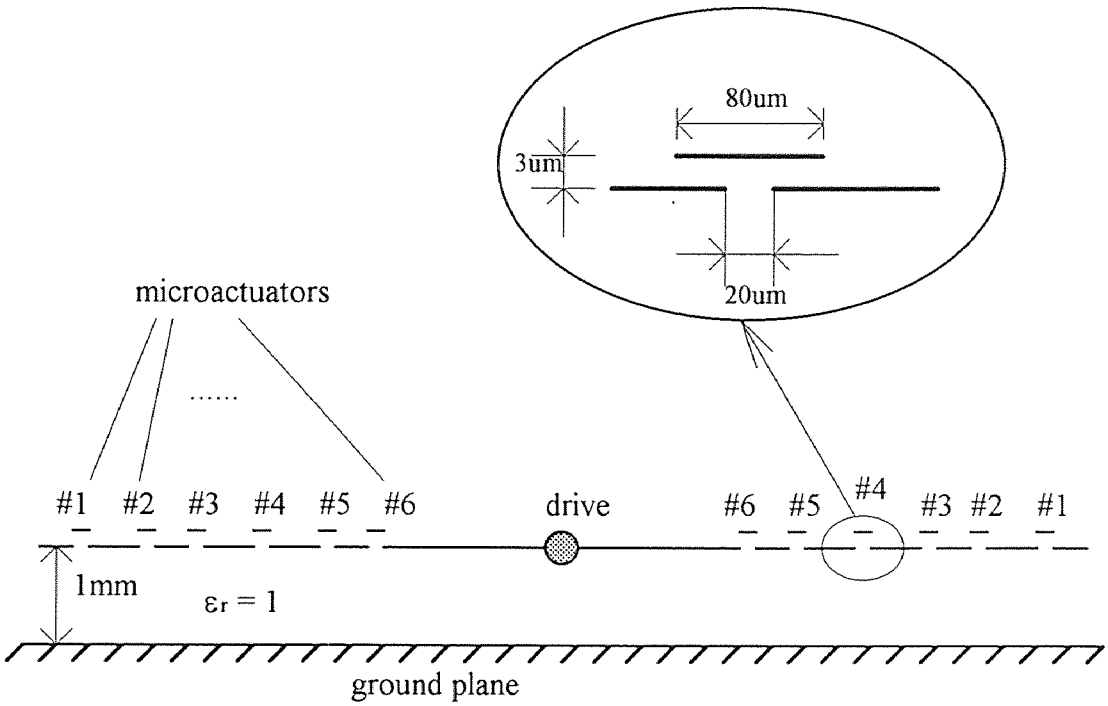

Figure 2.2 Cross-section of the model for I_NAC_3 simulation

An antenna software package I_NAC_3 is used to simulate the behavior of the antenna in Figure 2.2. The input impedance is calculated and plotted on the Input impedances . Simulation results are shown in Figure 2.3-2.6 and Table 2.1.

The Input impedance in Figure 2.3 shows characteristics of the antenna when it is at full length. The calculation is done at 11 different frequencies which are labeled from 1 to 11 on the Smith-Chart. The resonant frequency is obtained at the center (label 4), which is 18.5GHZ. The corresponding input impedance is 100Ω. Between 18.3GHZ and 18.7GHZ (label 3 to label 5), the standing wave ratio of the antenna is less than 1.2. This is the acceptable working range of this antenna. The bandwidth is only 2.2%, which is too small and can't satisfy the requirement of many applications.

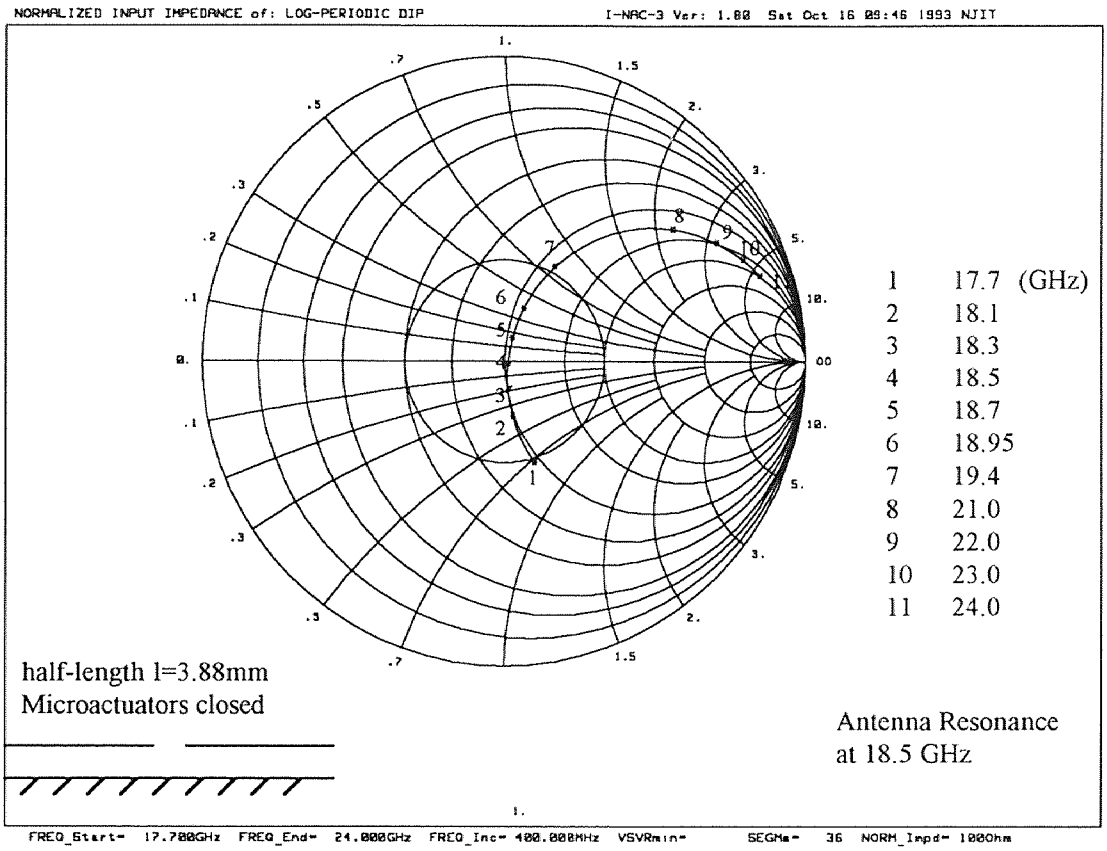

Figure 2.3 Smith-chart of input impedance of dipole antenna with l = 3.88mm
This pattern is corresponding to the antenna on ground plane in Figure 2.2. The antenna is placed 1mm above the ground. This result is based on $\varepsilon_r = 1$ for underlying dielectric half-space

The same normalized impedance of 100Ω is used in Figure 2.4-Figure 2.6. Figure 2.4 is the input impedance when actuator pair #1 is open circuit. The center frequency is changed to 18.92GHZ and the acceptable working range is from 18.7 to 19.15GHZ, where SWR < 1.2. This is a 2.4% bandwidth.

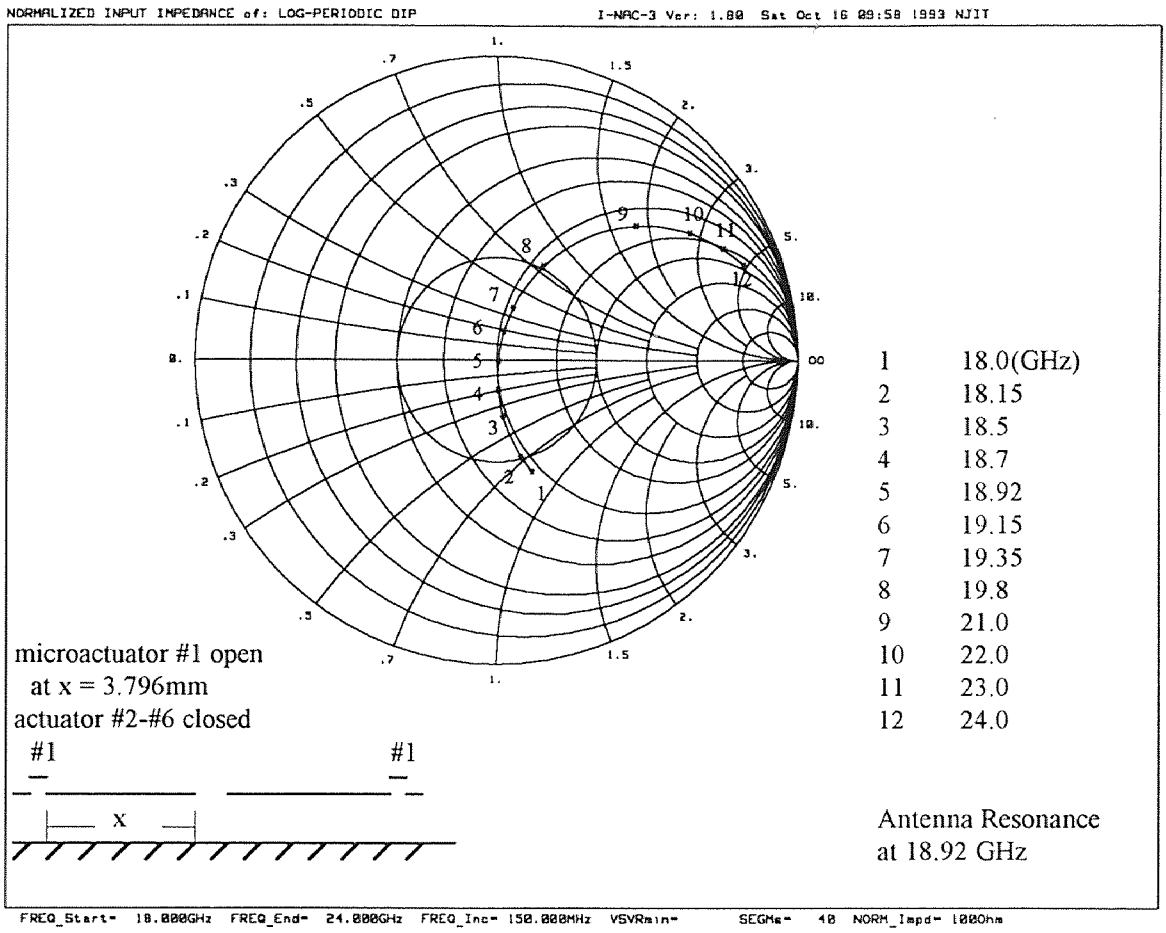

Figure 2.4 Smith-chart of input impedance with actuator #1 open and actuators #2-6 closed. This pattern is corresponding to the antenna on ground plane in Figure 2.2. The antenna is placed 1mm above the ground. This result is based on $\varepsilon_r = 1$ for underlying dielectric half-space

Figure 2.5 is the Input impedance when #1 and #2 are open circuit and the rest are short circuit. The frequency range satisfying the SWR < 1.2 is (19.15GHZ - 19.6GHZ). This is a 2.3% bandwidth.

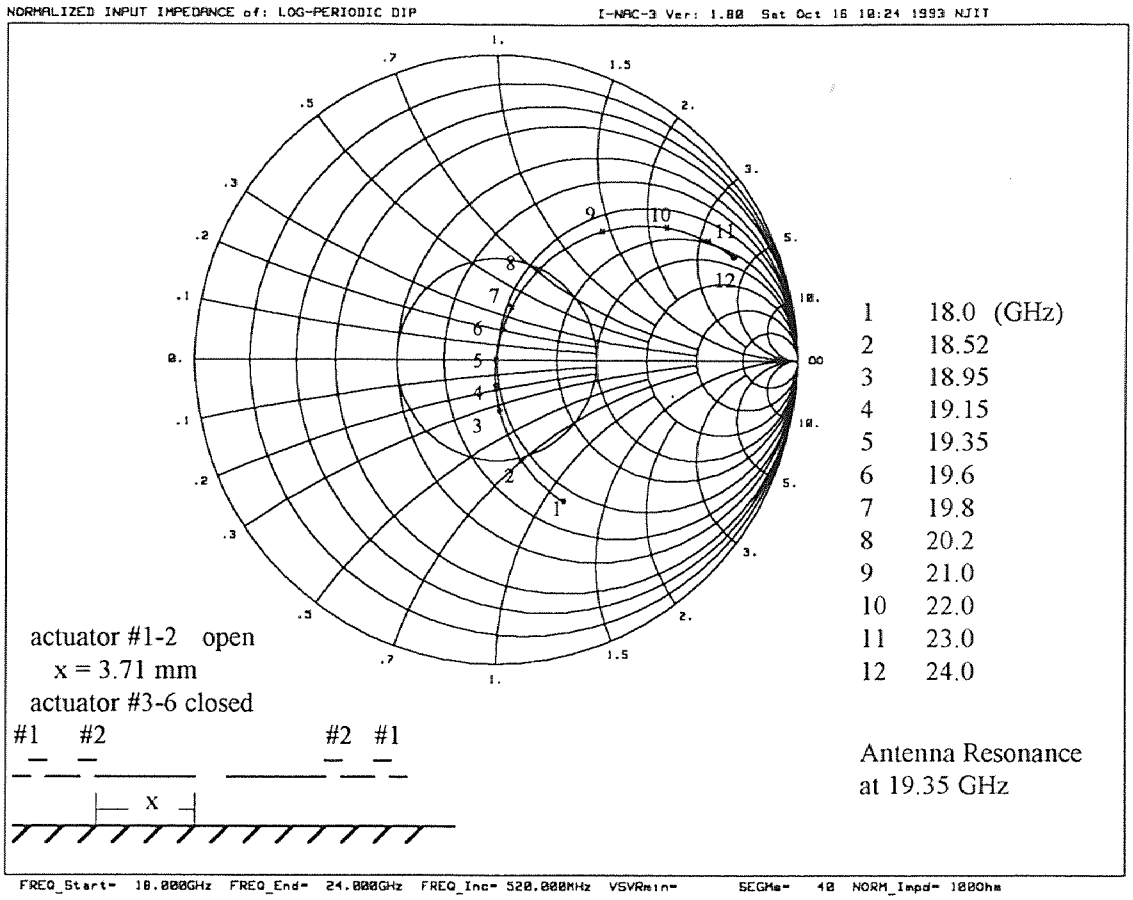

Figure 2.5 Smith-chart of input impedance with actuator #1-2 open and #3-6 closed. This pattern is corresponding to the antenna on ground plane in Figure 2.2. The antenna is placed 1mm above the ground. This result is based on $\varepsilon_r = 1$ for underlying dielectric half-space

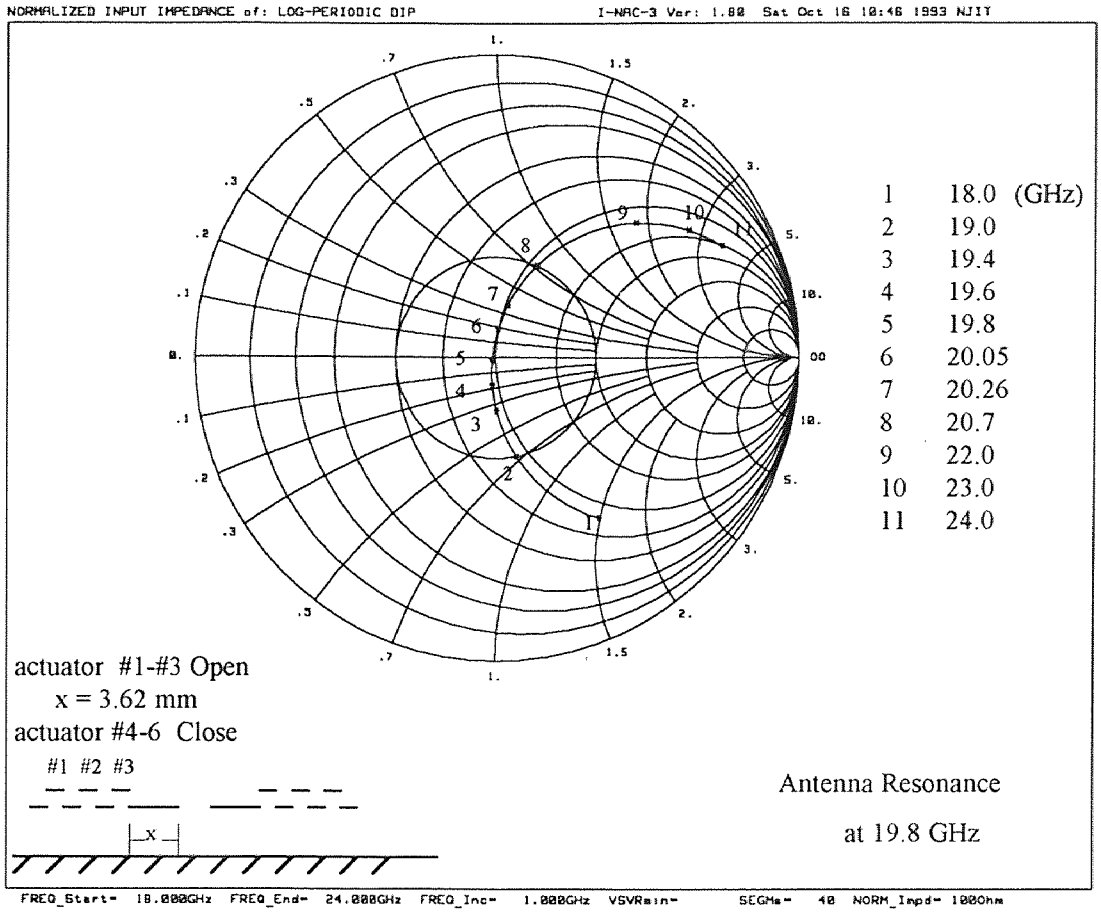

Figure 2.6 Smith-chart of input impedance with actuator #1-3 open and #4-6 closed. This pattern is corresponding to the antenna on ground plane in Figure 2.2. The antenna is placed 1mm above the ground. This result is based on $\varepsilon_r = 1$ for underlying dielectric half-space

When actuator #6 is open circuit and the rest are short circuit, the working frequency range is from 20.95 to 21.4GHZ. This is a 2.1% bandwidth. The continuity of all frequency ranges depends on the position of the actuator pairs. Since proper positions are chosen such that the antenna working frequency range are extended. The effective bandwidth of the programmable antenna with 6 pairs of actuators is 15.6%.

A summary of the simulation results and the antenna dimensions are given in Table 2.1.

Table 2.1 Resonant frequencies versus antenna lengths and standing wave ratios(VSWR) (l = 3.88 mm, a = 1um, Z_0=100Ω, ε_r=1)

Micro-actuator Open Circuit	Micro actuator is off at x(mm)	Resonate Frequency f_o(GHz)	Frequency Width with SWR < 1.2 from(GHz)	to (GHz)	Frequency Width with SWR < 1.4 from(GHz)	to (GHz)	Frequency Width with SWR < 2.0 from(GHz)	to (GHz)
None	3.88= l	18.5	18.3	18.7	18.1	18.95	17.7	19.4
#1	3.796	18.92	18.7	19.15	18.5	19.35	18.15	19.8
#1,2	3.71	19.35	19.15	19.6	18.95	19.8	18.52	20.0
#1-3	3.62	19.8	19.6	20.05	19.4	20.6	19.0	20.7
#1-4	3.54	20.26	20.05	20.5	19.85	20.7	19.4	21.2
#1-5	3.46	20.7	20.5	20.95	20.28	21.15	19.85	21.6
#1-6	3.38	21.15	20.95	21.4	20.75	21.65	20.3	22.1

Figure 2.7 shows the standing wave ratio change versus frequency for a length-fixed antenna and programmable dipole antenna. The programmable antenna has a 12% effective bandwidth, which is five times more than that of the length-fixed antenna. Each microactuator increases the controllable effective bandwidth of the antenna by approximate 1.7% around 20 GHZ center frequency.

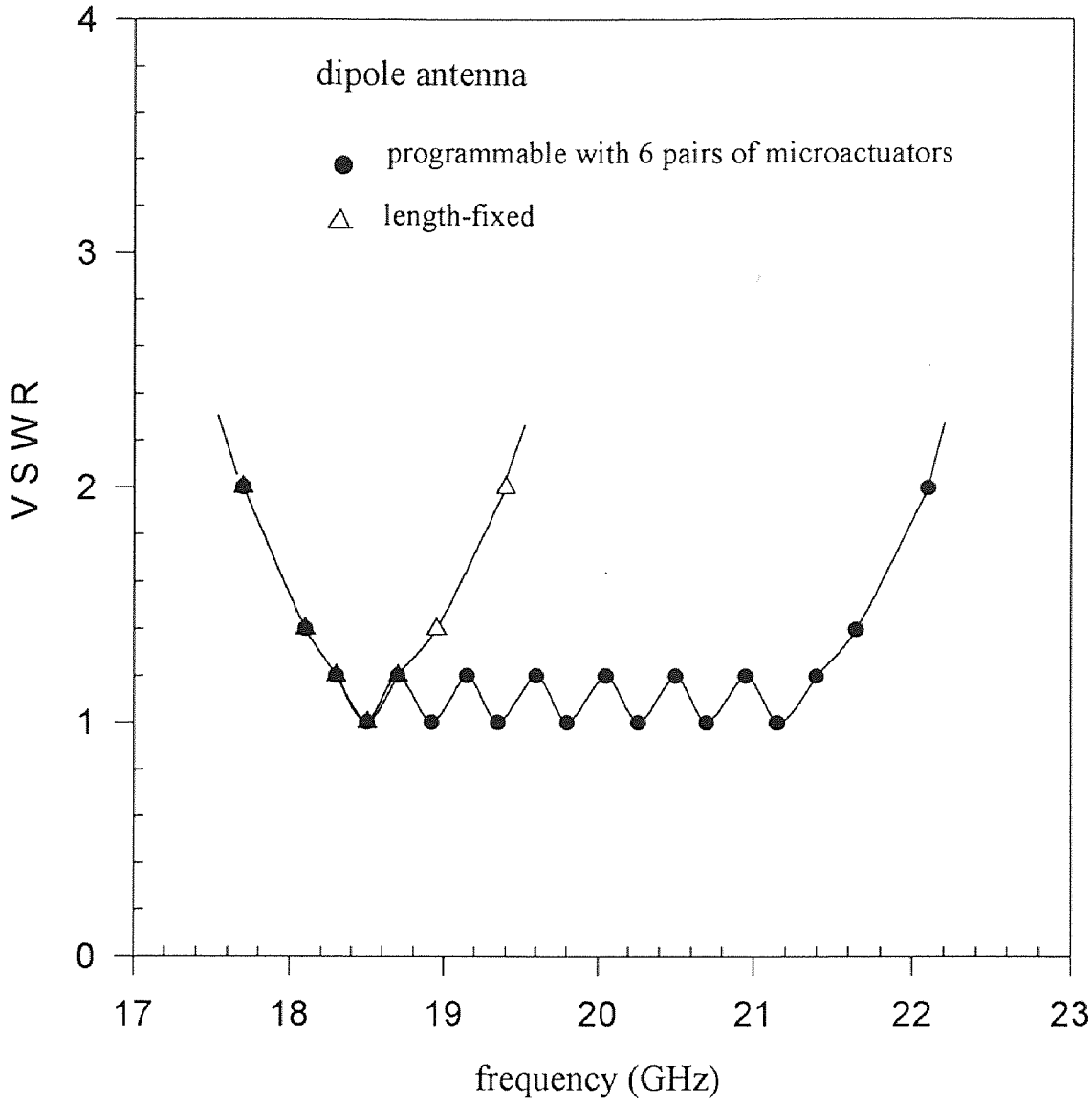

Figure 2.7 Comparison of antenna effective bandwidth for a length-fixed dipole and the programmable dipole(l_{max}=3.88mm, a=1μm,ε_r=1.0, Z_0=100Ω). This pattern is corresponding to the antenna on ground plane in Figure 2.2. The antenna is placed 1mm above the ground. This result is based on ε_r = 1 for underlying dielectric half-space

2.3 Effective Load Capacitance

The effective load capacitance caused by the discontinuity of the antenna arms and the microactuators has already been taken into consideration in I_NAC_3 simulation. The simulation result shows that the capacitance is very small and has negligible effect on the input impedance of the antenna. Figure 2.8 is the input impedance for a simple antenna(without microactuators) of l = 3.796mm. It is observed that Figure 2.8 has the same result as Figure 2.4 while Figure 2.4 is the Input impedance for a antenna with microactuators. Based on this observation, the capacitance can be neglected when calculating the input impedance of the programmable antenna.

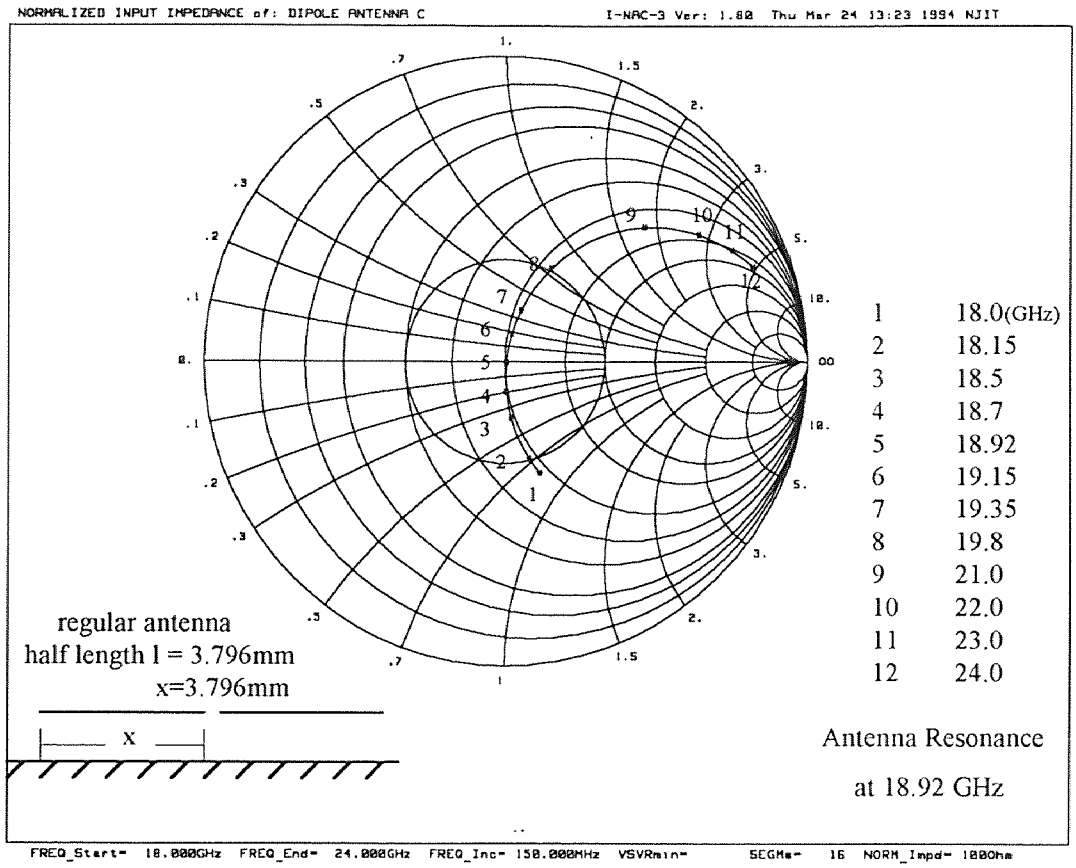

Figure 2.8 Smith-chart of a length-fixed dipole(without gap and microactuators, l_{max}=3.796mm, a=1μm,ε_r=1.0, Z_0=100Ω). This pattern is corresponding to the antenna on ground plane in Figure 2.2. The antenna is placed 1mm above the ground. This result is based on ε_r = 1 for underlying dielectric half-space

2.4 Radiation Pattern of Dipole Antenna

The radiation pattern of a center-driven cylindrical antenna in general depends upon its length and thickness. In order to calculate the radiation pattern, first of all the proper choice of expression functions for the current distributions must be chosen. Sinusoidal expansion functions are used because of the following reasons:

1) the boundary conditions for the antenna current distribution are automatically satisfied;

2) a closed-form expression for the field is obtained.

Thus with an assumed current distribution of the form

$$I(x) = I_0 \sin k(l - |x|) \qquad l \geq x \geq -l \tag{2.3}$$

the radiation field, expressed in spherical coordinate system, is given by[10]

$$E_\theta = \frac{j\eta}{2\pi} \frac{I_0 e^{jkR}}{R} \left[\frac{\cos(kl\cos\theta) - \cos kl}{\sin\theta} \right] \tag{2.4}$$

where $\eta = (\mu/\varepsilon)^{1/2} = 120\pi\ \Omega$

θ = angle measured from axis of dipole, or x axis

The radiation patterns of both length-fixed antenna shown in Figure 2.1 and programmable antenna shown in Figure 2.2 are calculated. The results are shown in Figure 2.9 and Figure 2.10 respectively. Figure 2.9 and Figure 2.10 are compared and it is observed that the programmable microstrip antenna in Figure 2.2 has almost the same radiation pattern as the length-fixed one in Figure 2.1. The length-fixed antenna is of a gain -1.97 dB, 3dB bandwidth 30.42° and 45.73° in E-plane and H-plane respectively,

while the programmable antenna is of a gain -1.74 dB, 3dB bandwidth 30.44° and 45.77° in E-plane and H-plane respectively.

The following conclusions can be drawn from the above comparison: The actuators and the antenna arm discontinuities have negligible effect on the radiation pattern. The actuation does not affect the 100(Ohm) antenna impedance when frequency changes if proper actuation positions are chosen. This can maintain acceptable small VSWR.

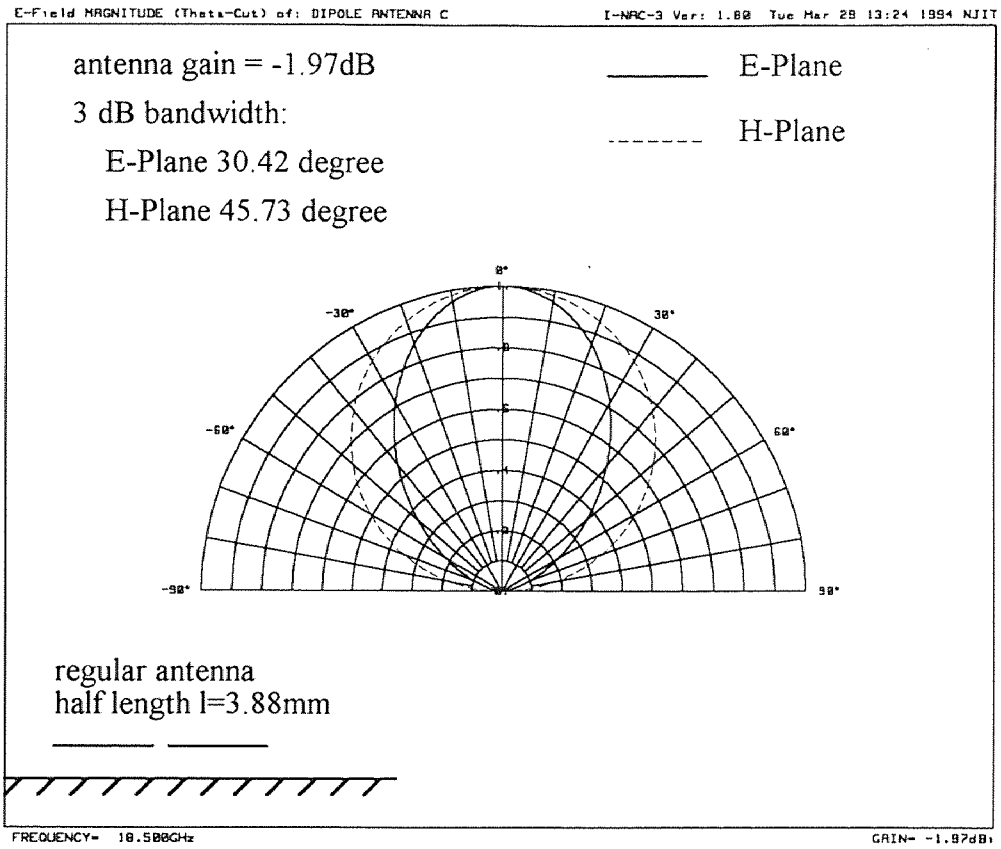

Figure 2.9 Radiation pattern of a length-fixed dipole antenna (l = 3.88mm, a=1μm)
This pattern is corresponding to the antenna on ground plane in Figure 2.2. The distance from the ground is 1mm. This result is based on $\varepsilon_r = 1$ for underlying dielectric half-space

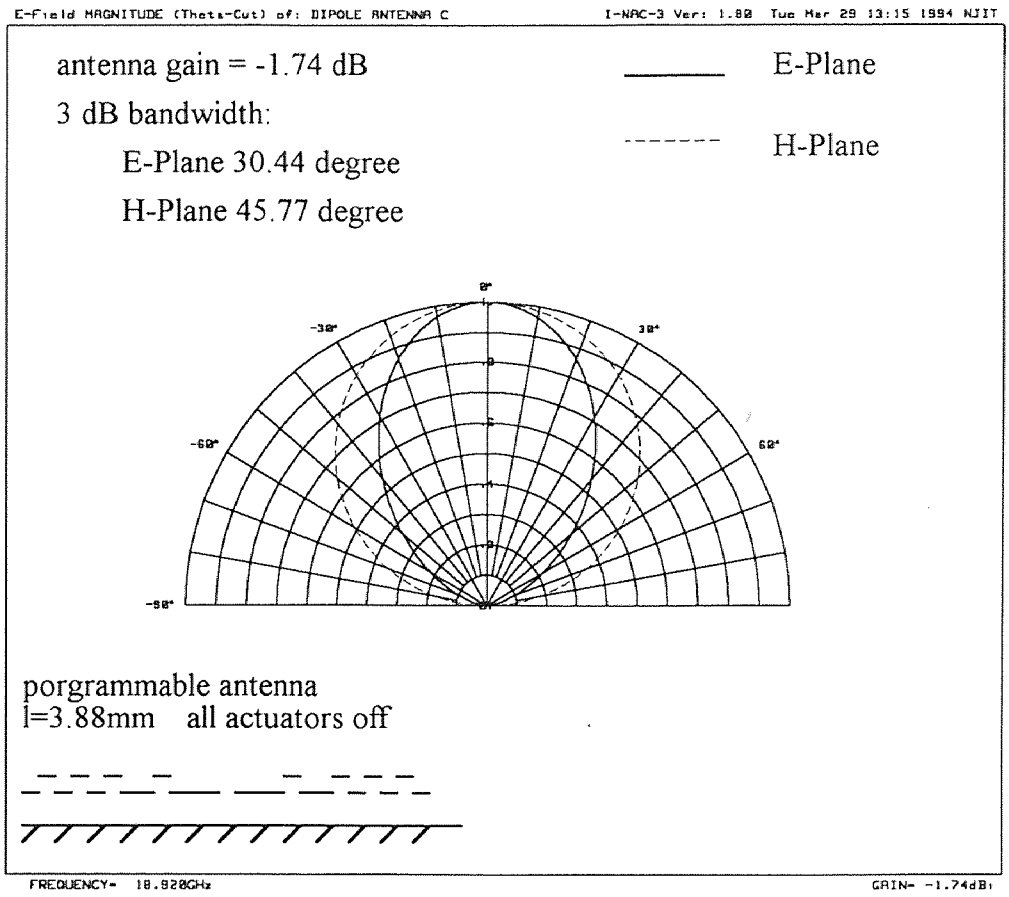

Figure 2.10 Radiation pattern of a programmable antenna(l = 3.88mm but with actuators open). This pattern is corresponding to the antenna on ground plane in Figure 2.2. The distance from the ground is 1mm. This result is based on ε_r = 1 for underlying dielectric half-space

2.5 Equivalent Radius of Rectangular Cross Sections

Since the simulator I_NAC_3 is based on circular wire antenna elements. The modeling for a strip dipole antenna requires careful consideration since it has a rectangular cross-section. In the following an equivalent circular cross section is derived for the actual antenna which is rectangular cross-section. As far as the impedance characteristics and radiation pattern are concerned, a thin antenna with a rectangular cross section behaves like a circular cylindrical antenna with an equivalent radius[10]. The equivalent radius of many simply shaped cross sections can be found by the method of conformal mapping. For

a rectangular cross section the result is plotted in Figure 2.11. The equivalent radius a_{eq} of a rectangle is a function of the ratio of thickness t to width s. Therefore the problem of antennas with rectangular cross-section can be transformed to the problem of wire antennas.

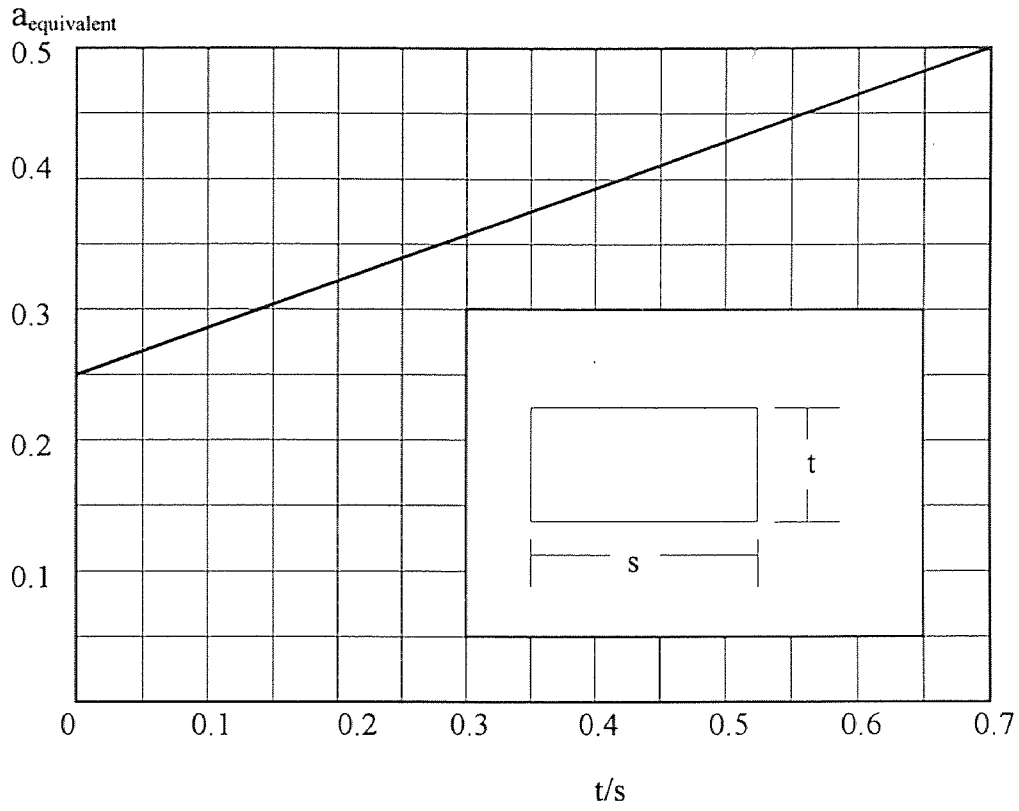

Figure 2.11 Equivalent radius of antenna cross-section rectangle(units normalized)[10]

2.6 Radiation Pattern and Input Impedance of Printed Dipoles

The discussion in previous section are based on antennas in free space although the ground are introduced into the simulation model in Section 2.2. The detailed discussion on the microstrip dipole antenna is presented in this section. Another simulator called SMAD is used to calculate the impedance of microstrip dipole antennas.

Figure 2.12 and Figure 2.13 show the microstrip dipole antenna and printed wire antenna respectively. The difference between them is in the cross section of the antenna. The one in Figure 2.12 is with rectangular cross section and the other one in Figure 2.13 is with circular cross section.

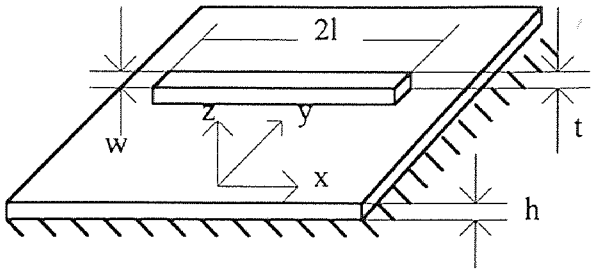

Figure 2.12 Microstrip dipole antenna

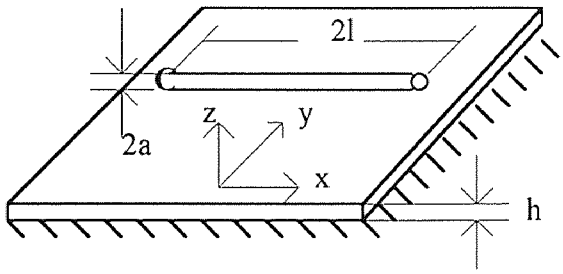

Figure 2.13 Printed wire dipole antenna

Consider a microstrip dipole antenna in Figure 2.12. This dipole is of length $2l$, width w and thickness t. The substrate is of thickness h.

According to the discussion in Section 2.5, the microstrip width w can be transformed into the radius of a wire dipole in Figure 2.13. Then same method can be used to compute the radiation pattern and input impedance for both cases.

The current distribution , input impedance and radiation pattern have been calculated [11] using moment method. The procedure is included in Appendix A.

The input impedance if the printed wire dipoles for a 1.0 V input excitation is given by

$$Z_{in} = 1.0 / I_{in} \tag{2.5}$$

where I_{in} is the current at the input terminals of the antenna, which has been solved(Appendix A).

The SMAD program is performed to calculate the input impedance of a thin microstrip dipole . The result is shown in Figure 2.14. This result is consistent with the previously published result for a printed wire dipole[11].

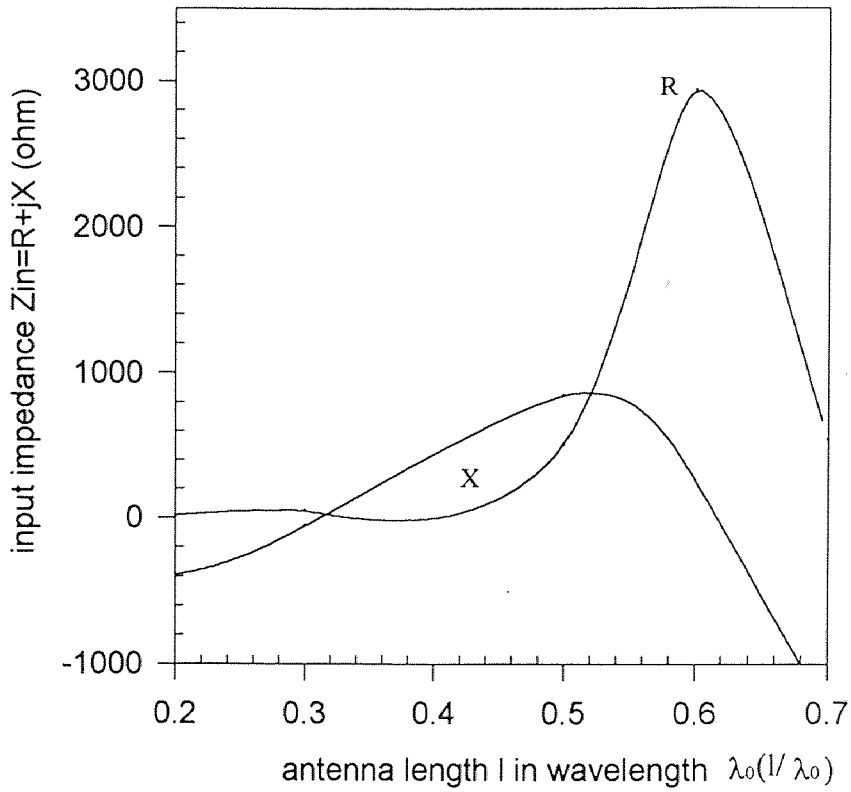

Figure 2.14 Input impedance of a microstrip dipole antenna versus length l (ε_r=3.25, h=0.0127λ_0, a_{eq}=0.00005λ_0)

2.7 Conclusions of This Chapter

The input impedance and radiation patterns of the dipoles in free space and on grounded substrate are discussed in this chapter. Following conclusions can be drawn from the computations and simulations which have been done:

1) The resonant frequency of the dipole antenna can be changed efficiently by changing its length.

2) The length changing of the antenna can be realized by external control of the microactuators. This technique will adjust the input impedance but won't affect the shape of the radiation pattern.

3) The capacitance caused by the antenna discontinuities and microactuators have negligible efface on the input impedance and radiation pattern of the programmable antenna. The fixed-length microstrip dipole antenna mode can be employed to accurately calculate the input impedance for programmable antenna.

CHAPTER 3

PROGRAMMABLE MICROSTRIP ANTENNA DESIGN

3.1 A Fixed-length (non-Programmable) Microstrip Dipole Antenna

Fixed-length (nonprogrammable) microstrip dipole antenna is designed as the prototype of the programmable one. Figure 3.1 is a schematic view of a non-programmable microstrip dipole. The dipole is a very thin layer (0.5um-1.5um thickness) on the top of a high resistivity silicon substrate. The bottom side of this substrate is coated with a thin metal film. The dipole is shown with a coplanar microstrip feedline. The dimensions of this antenna are listed in Figure 3.2.

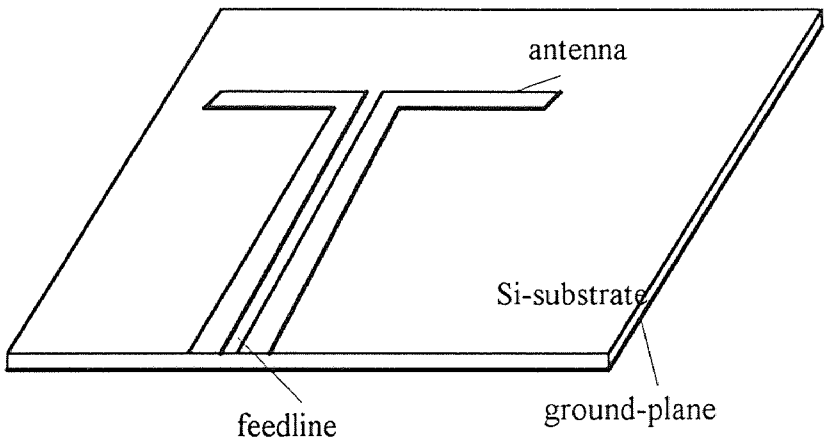

Figure 3.1 A microstrip dipole antenna with feedline

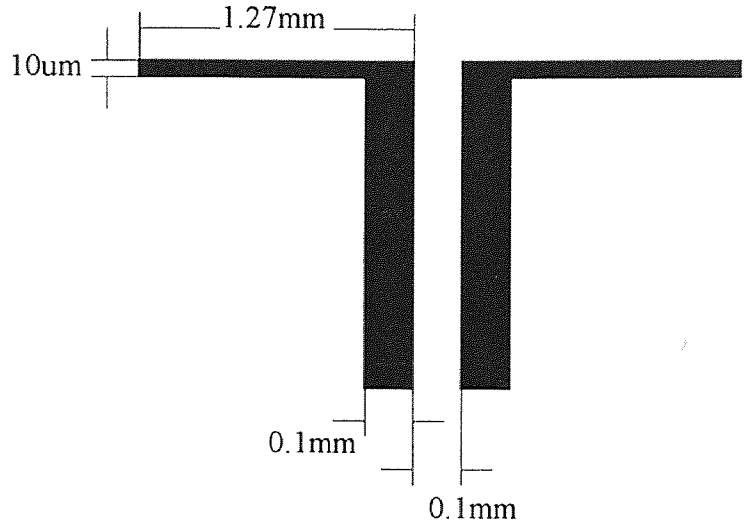

top view

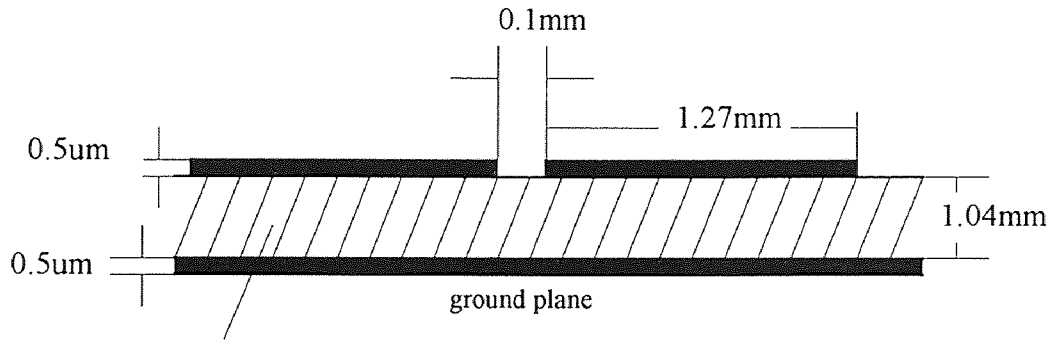

cross-section view

Figure 3.2 Top view and cross-section view of the microstrip dipole antenna

The input impedance of this antenna was calculated by using the program SMAD for the microstrip antenna. The resistance and reactance versus the frequency are plotted in Figure 3.3 and Figure 3.4 respectively. It is shown that the resonant frequency is 19.84GHZ. The input impedance of the antenna at resonance is 44Ω. This antenna is excited through the coplanar microstrip line. It is known that this kind of transmission line with w = s = 0.1mm has characteristic impedance of $Z_0 = 44\Omega$. The theoretical standing wave ratio VSWR is equal to 1 at resonant frequency(19.84GHZ).

The bandwidth for the standing wave ratio VSWR < 1.2 can be calculated. Smith-chart is utilized here. The input impedances versus frequency are plotted on the Smith-chart. Two points which present the impedances at the circle of VSWR=1.2 are found. The corresponding frequencies are the lower and upper bond of the bandwidth. The fixed-length dipole has a VSWR < 1.2 from 19.79GHZ to 19.88GHZ. The bandwidth is only 0.5%. This is a very limited bandwidth for most applications.

The bandwidth can also be calculated using (3.1) and (3.2) . They are essential formulas for calculating the reflection coefficient ρ and the standing wave ratio *VSWR*. The standing wave ratio can be obtained from (3.1) and (3.2) using the data in Figure 3.3 and Figure 3.4.

$$\rho = \frac{Z_{in} - Z_0}{Z_{in} + Z_0} \tag{3.1}$$

and

$$VSWR = \frac{1+|\rho|}{1-|\rho|} \tag{3.2}$$

where Z_{in} is the input impedance of the antenna,

Z_0 is the characteristic impedance of transmission line.

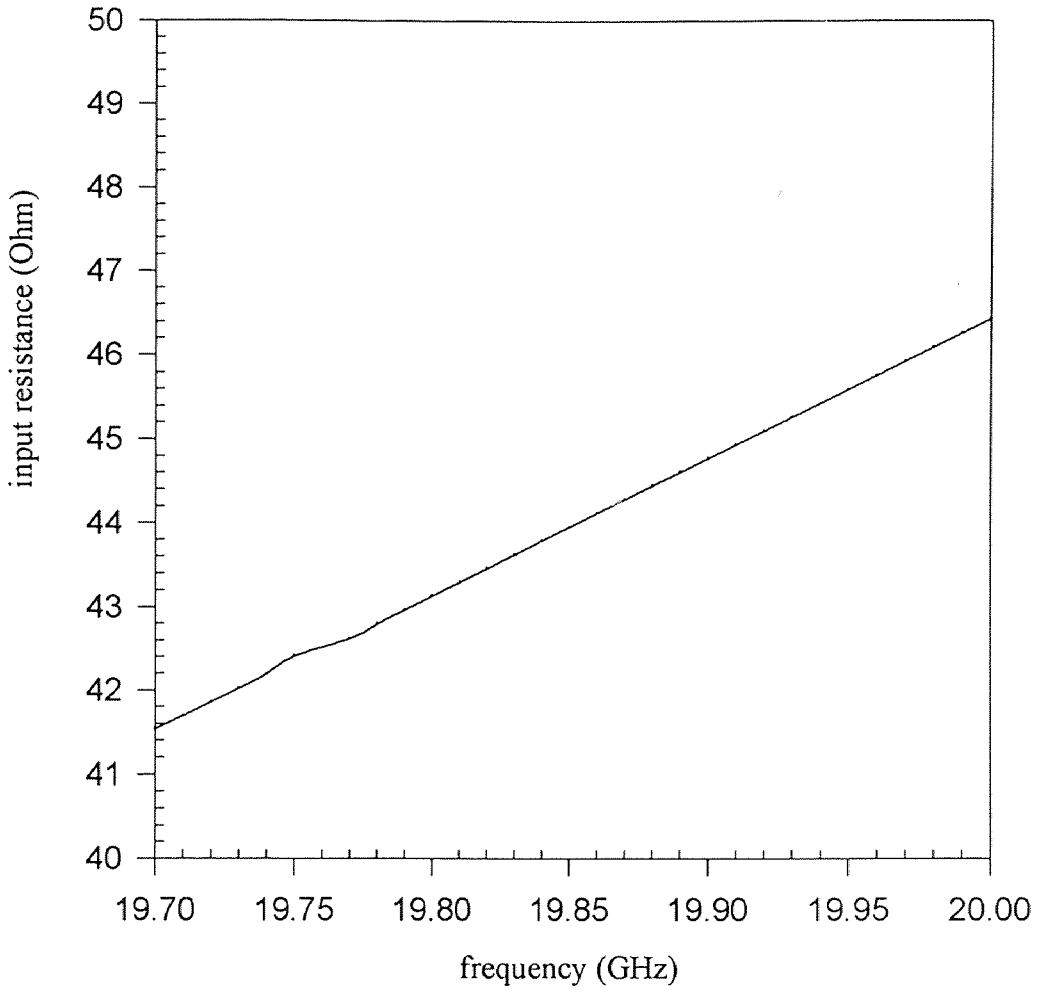

Figure 3.3 Input resistance of the fixed-length microstrip dipole antenna versus frequency(ε_r=12)

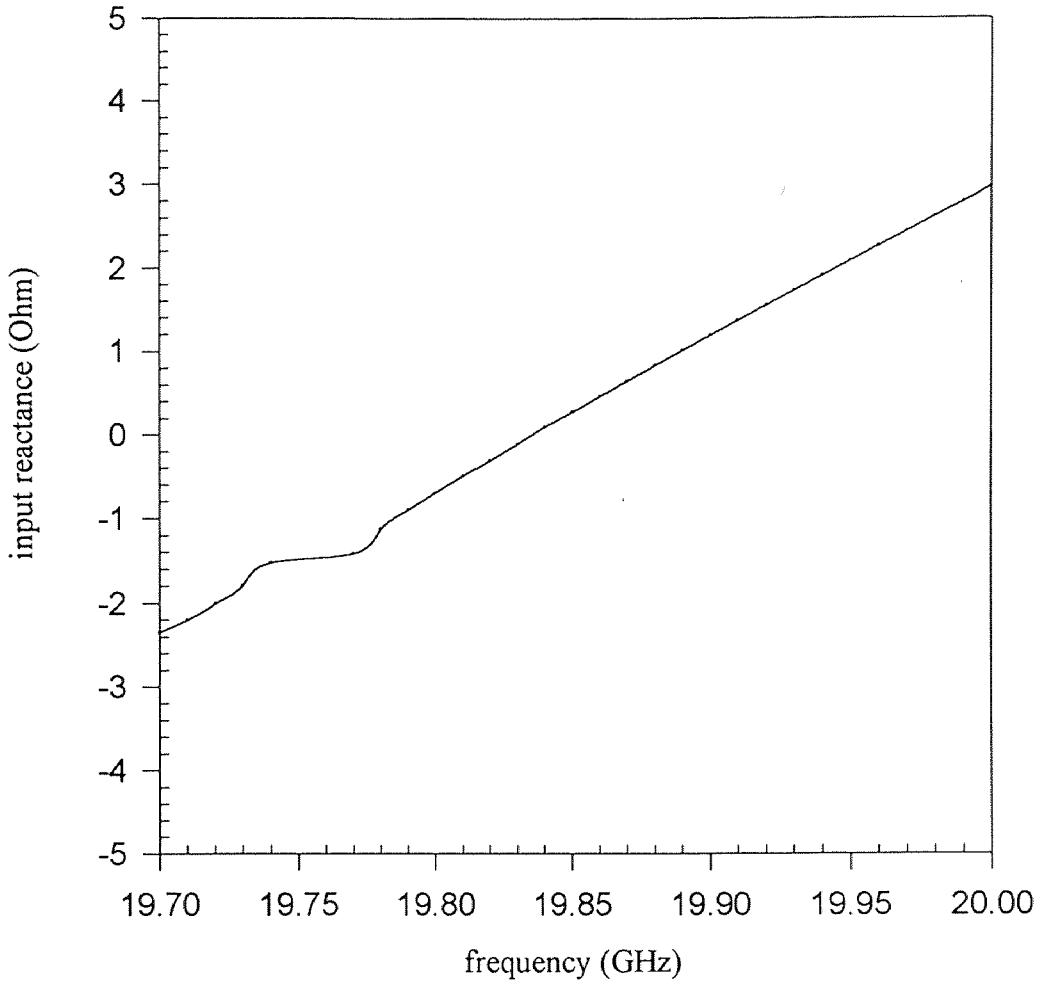

Figure 3.4 Input reactance of the fixed-length microstrip dipole antenna versus frequency(ε_r=12)

3.2 Programmable Microstrip Dipole Antenna Design

In order to increase the effective bandwidth of microstrip dipole antenna, a microactuator controlled antenna is designed. A schematic view of the programmable antenna with two microactuators on each arm is shown in Figure 3.5.

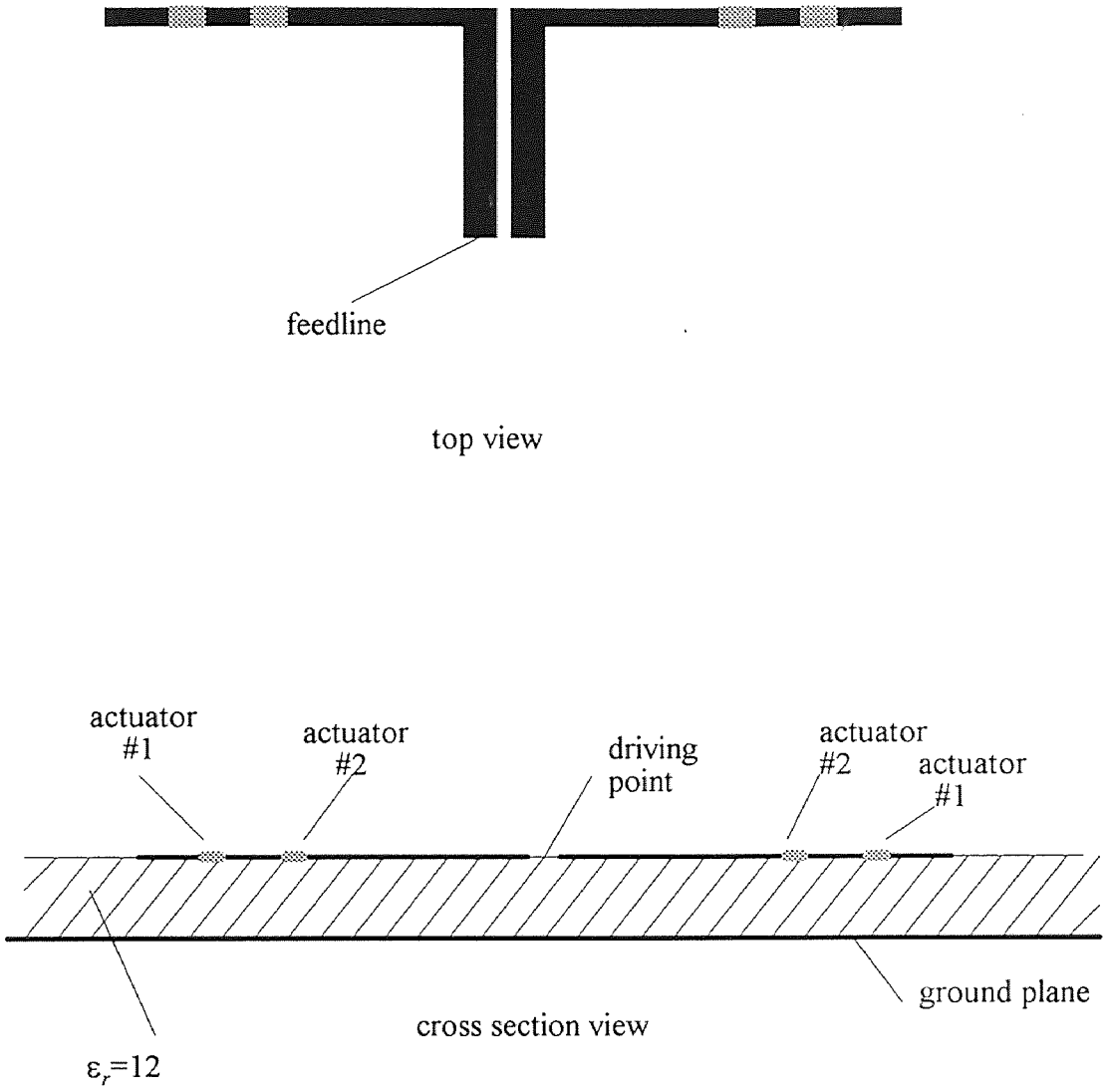

Figure 3.5 Schematic view of a programmable microstrip dipole

A non-programmable antenna has been designed in the previous section. It works with a standing wave ratio VSWR < 1.2 in the range of f_L=19.79GHZ to f_H=19.88GHZ. The procedure for designing a programmable antenna based on this non-programmable one is summarized as following :

1) Increase the antenna half length to l', which is also the distance between the microactuator and the center driven point of the antenna

2) Find the input impedance versus frequency

3) Find the new frequency f_H' and f_L' so that the standing wave ratio VSWR is less than 1.2 from f_H' to f_L'

4) The position is found if $f_H' = f_L$

5) if $f_H' \neq f_L$, adjust the antenna length. There are two cases:

if $f_H' < f_L$, decrease the length

If $f_H' > f_L$, increase the length

Then go to step 2.

SMAD for the microstrip antenna has been run with different antenna lengths to search the proper positions of the microactuator. The position for microactuator #2 was obtained through above procedure. The same technique was used to get the position of microactuator #1 and the maximum length of the antenna. When microactuator #2 closed the working frequency range is 19.69-19.79GHZ. When microactuator #1 is also closed, the working frequency is 19.59-19.69GHZ. The design results are summarized in Table 4.1. The working frequency range covers from 19.59 to 19.88GHZ. This programmable antenna with two microactuators on each arm has been shown in Figure 3.5. The antenna dimensions and microactuator positions are shown in Figure 3.6. The details of microactuator structures will now be discussed in the next section.

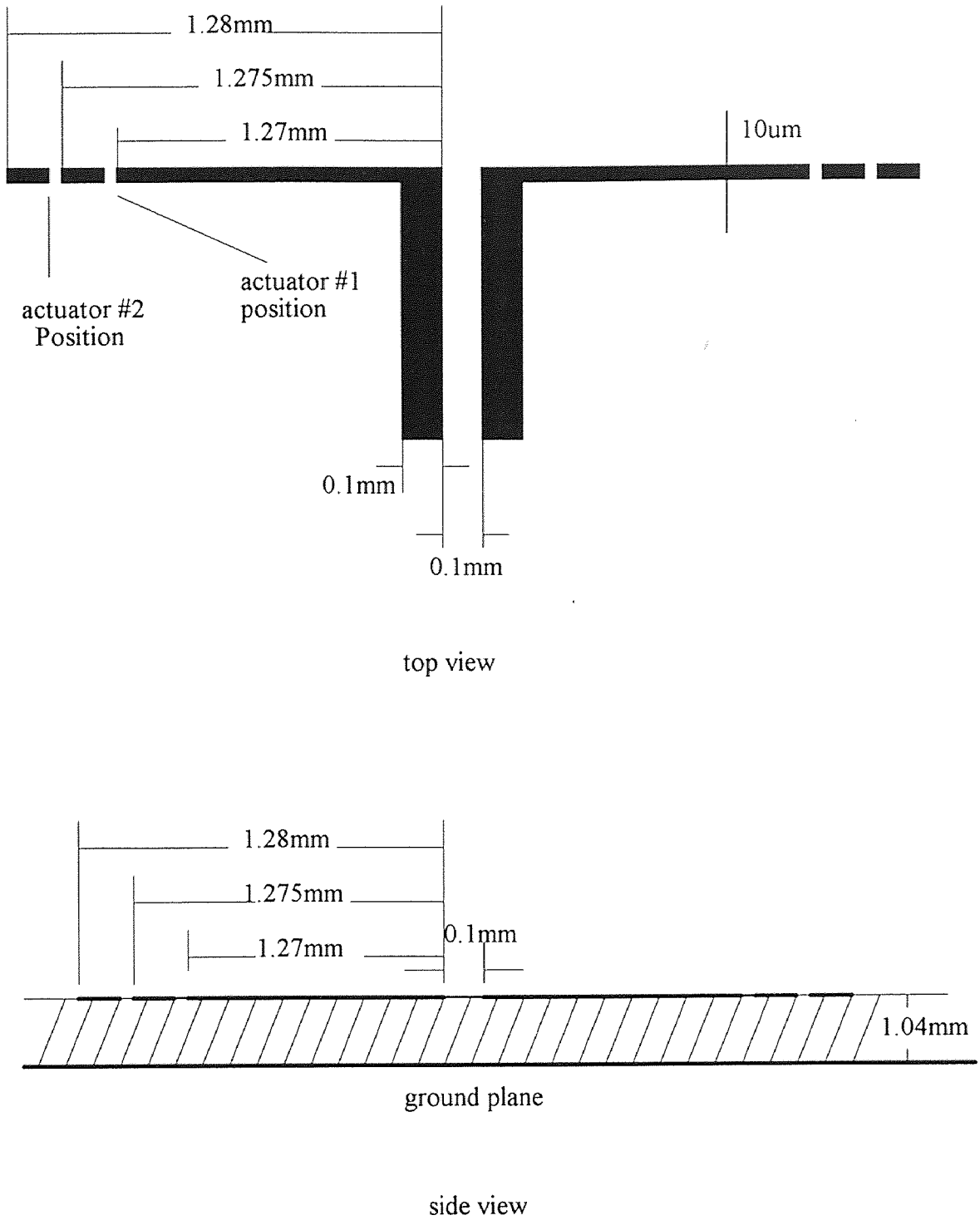

Figure 3.6 A designed programmable microstrip dipole antenna with two microactuator positions

Table 3.1 Programmable antenna design results for antenna in Figure 3.6

actuated	position l'(mm)	function
none		basic fixed dipole frequency range: 19.79-19.89Ghz
#1	1.27	working frequency range: 19.69-19.79GHz
#2	1.275	working frequency range: 19.59-19.69GHz

3.3 Conclusions of This Chapter

Programmable microstrip antenna with two pairs microactuators was designed. The range of working effective bandwidth is increased to 2.0% from 0.5% for the fixed length dipole. Each actuator permits an increase of antenna effective bandwidth of approximately 0.75%. This effective bandwidth can be increased further as more actuators are added.

CHAPTER 4

THERMAL MICROACTUATORS

4.1 Introduction

The microelectromechanical switches provide the basis for the programmable antenna. There are several designs that can be used for the micro electro mechanical switches. Frequently used microactuation methods have been based upon electromagnetic [12][13] [7], piezoelectric [14], and thermal [4][6] effects.

Figure 4.1 Simple beam microactuator structure

Figure 4.2 Cantilever beam microactuator structure

The electromagnetic microactuator can be used but it is difficult to realize monolithic integrated actuators. The thermal actuators are chosen for the programmable antenna. This kind of actuator is based on the so-called bimetal effect used extensively for the fabrication of temperature-controlled electrical switches. Generally, materials of different thermal expansion are combined in a sandwich structure. When the temperature goes higher, the structure will bend to the direction of either layer because of the difference between the expansion coefficients.

Thermal bimetallic simple beam and cantilever beam are common. These structures are shown in Figure 4.1 and Figure 4.2 respectively. The dashed line represents the movement of the beam when thermally excited. The beam can only either bend up or bend down depending on the materials.

It is shown in Figure 4.1 that both ends of the simple beam are fixed. The beam can pop up or bend down when it is thermally excited. Figure 4.2 shows that the cantilever beam has a free end. The free end of the cantilever will bend up or bend down when heated. Both simple beam and cantilever beam contain at least two layers. The bending direction depends on the physical properties of the combined layers.

The physical properties of some materials of consideration are tabulated in Table 4.1. The best values for the difference in the thermal expansion coefficients are achieved by combing Poly-Si, Si or SiO_2 with metals like Pb, Al, Au or Pd.

There are following advantages with these thermal microactuators:

1) the beam deflection is directly coupled with the dissipated electrical power and, therefore, the device can be operated at standard microelectronic voltage levels;
2) the transducer elements exhibit a high mechanical rigidity;
3) the fabrication process is simple and fully compatible to standard IC production steps;
4) the whole device is fabricated with a single wafer process, and no additional bonding or mounting techniques are necessary to create an operating device

Table 4.1 Physical constants for potential microactuator materials based on thermal expansion[4]

Material	Thermal Coefficient of Expansion $[10^{-6}/K]$	Young's Modulus $[10^{11} Pa]$	Specific Heat $[10^{3} J/kgK]$	Thermal Conductivity $[W/mK]$	Density $[10^{3} kg/m^{3}]$
Si	2.6	1.62	0.691	170	2.42
SiO_2	0.4	0.74			2.66
Si_3N_4	2.8	1.55		18.5	3.44
SiC	3.5	4.57		86.5	3.2
Poly-Si	2.33	1.69	0.754		2.33
Al	23.0	0.69	0.9	235	2.692
Au	14.3	0.8	0.129	318	19.4
Pt	8.9	1.47	0.133	73	21.5
Cu	16.7	0.12	0.387	401	8.95
Ni	12.8	2.1	0.444	91	9.04
Pb	28.7	0.16	0.128	35	11.48
Pd[33]	13	1.67			

and

5) the actuator structure can be combined with sensing elements monitoring the center band setting of the microelectromechanical antenna device.

4.2 Characteristics of Bimorph Simple Beam

Some silicon actuators consist of a Si-metal sandwich layer as a moving (bending) element. An integrated poly-Si heating resistor on Si as the driving element. While some of them simply contain poly-Si and metal. poly-Si acts as both moving element and driving element. Due to the low heat capacity of the transducer element, a high increase of temperature in the actuator per input power unit can be achieved.

Figure 4.3 shows a bimorph simple beam structure. The two materials forming the action beam are labeled as 1 and 2 respectively. Material 1 and material 2 are combined together, which are with different thermal expansion coefficients α_1 and α_2, respectively. Assume that both layers have the same length at the room temperature. Left end and right end of this beam are fixed.

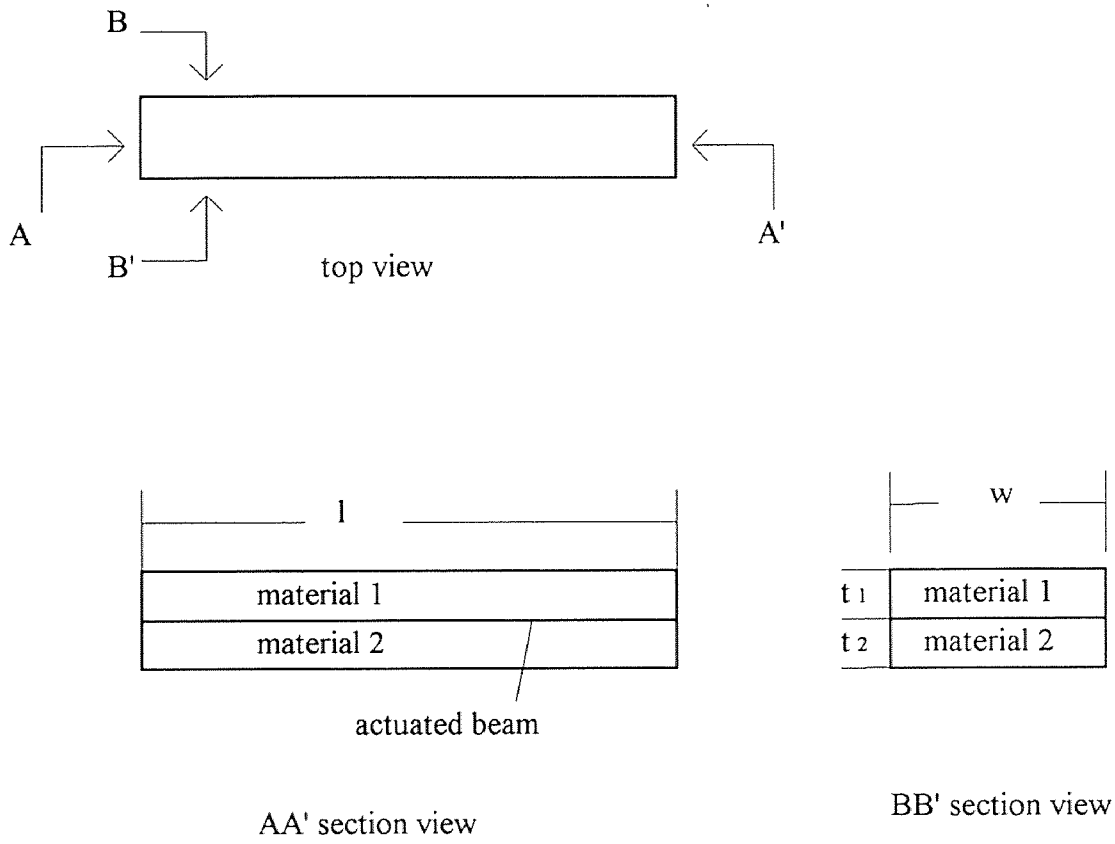

Figure 4.3 A bimorph Simple Beam Structure

The center deflection d of a simple beam can be derived using the linear(dotted line) model in Figure 4.4. Figure 4.4 is a schematic of a simple beam. The original length of the beam is $2r_0$, which becomes approximately $2r_1$ when a the beam is heated with respect to the substrate and a deflection d at the center of the beam occurs.

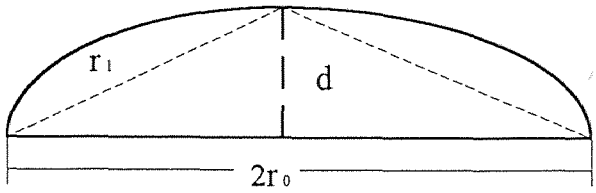

Figure 4.4 Schematics showing the linear approximation used for the center deflection calculation

The simple beam length change is proportional to the temperature change ΔT and the difference $\Delta\alpha$ between the thermal expansion coefficients α_1 and α_2. This relationship is expressed in (4.1).

$$r_1 - r_0 = \Delta\alpha \cdot \Delta T \cdot r_0 \tag{4.1}$$

since $r_1^2 = d^2 + r_0^2$, and the term of $O(\Delta^2\alpha)$ can be neglected, (4.2) is obtained:

$$r_1^2 \approx r_0^2(1 + 2\Delta\alpha \cdot \Delta T) \tag{4.2}$$

or:

$$\left(\frac{d}{r_0}\right)^2 = 2\Delta\alpha \cdot \Delta T \tag{4.3}$$

formula (4.3) can also be expressed as:

$$d = l\sqrt{\frac{\Delta\alpha\ \Delta T}{2}} \tag{4.4}$$

where $l = 2r_{0,}$ which is the length of the beam.

Formula (4.4) shows that the deflection is proportional to the length and square root of the difference between expansion coefficient of two layers and the temperature change. This equation is often used to estimate the center deflection d of the simple beam.

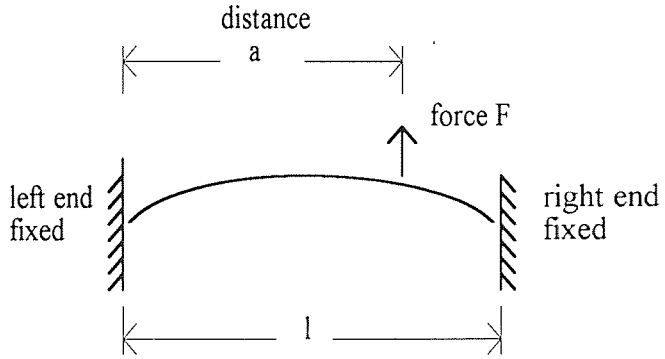

Figure 4.5 A left end and right end fixed simple beam

The following formulas can be used to calculate the force of any point at the beam.[30]. These equations are corresponding to Figure 4.3 and Figure 4.5. The structure is left end fixed and right end fixed as shown in Figure 4.5. These force F values refer to the case where d = 0 and where $\Delta T \neq 0$.

$$F = \frac{6\ EI\ a(l-a)\Delta\alpha\ \Delta T}{(t_1+t_2)l^3} \tag{4.5}$$

with

$$EI = \frac{w\ t_2^3 t_1 E_2 E_1}{12(t_1 E_1 + t_2 E_2)} K_1 \tag{4.6}$$

where E_i is Young's modulus

t_i is the thickness of the respective layer

w is the width of the layers

K_1 is the equivalent geometry coefficient(no unit)

$$K_1 = 4 + 6\frac{t_1}{t_2} + 4\left(\frac{t_1}{t_2}\right)^2 + \frac{E_1}{E_2}\left(\frac{t_1}{t_2}\right)^3 + \frac{E_2}{E_1}\frac{t_2}{t_1} \tag{4.7}$$

Figure 4.6-4.8 are a set of figures to show the center deflections and forces for different bimorph simple beam structures. Useful constants for calculation are listed in Table 4.2.

Table 4.2 Useful constants for calculating deflection and force

material 1	thermal coefficient of expansion α_1 [10^{-6}/°C]	Young's modulus E_1 [10^{11}Pa]
Al	23	0.69
Au	14.3	0.8
Pd	13	1.67
Pt	8.9	1.47
material 2	thermal coefficient of expansion α_2 [10^{-6}/°C]	Young's modulus E_2 [10^{11}Pa]
Poly-Si	2.33	1.69

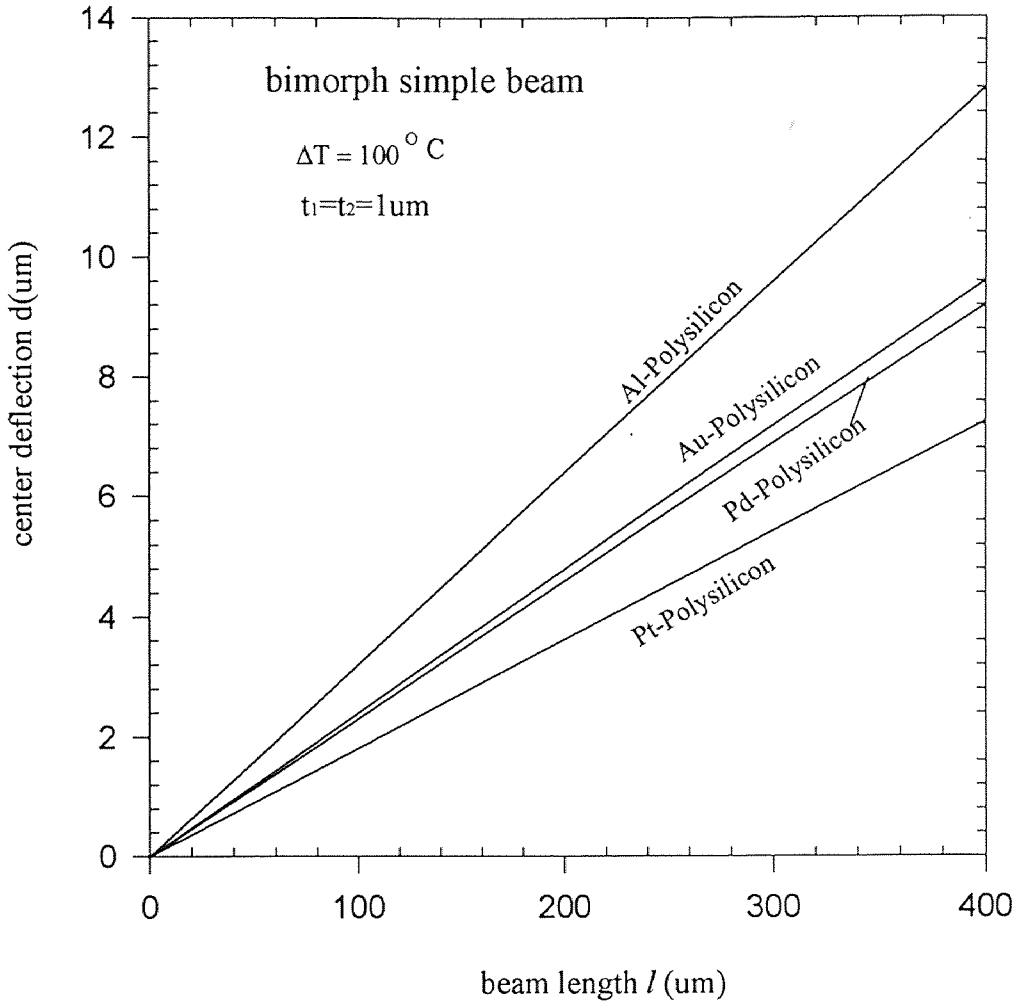

Figure 4.6 Center deflection d versus length *l* for different bimorph simple beams based on the first order model of equation (4.4)

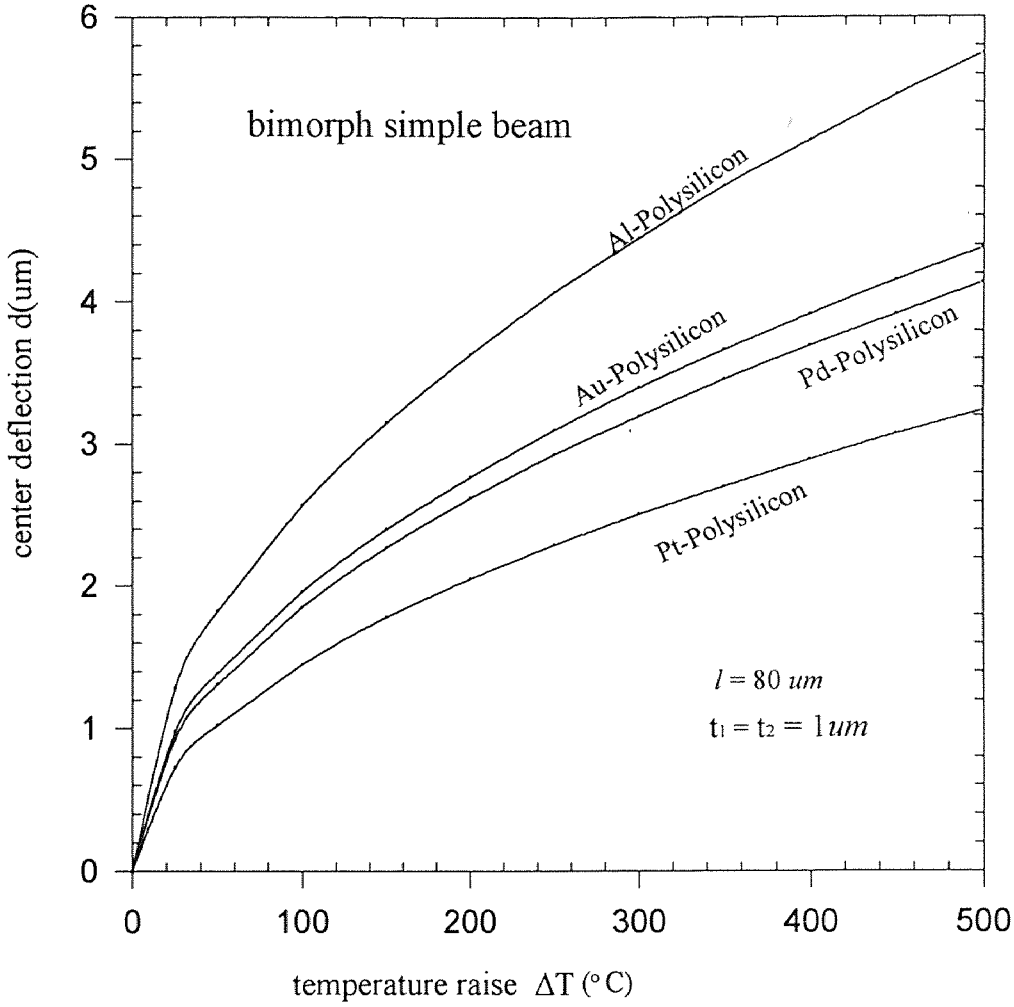

Figure 4.7 Center deflection versus ΔT(°C) for different bimorph simple beams

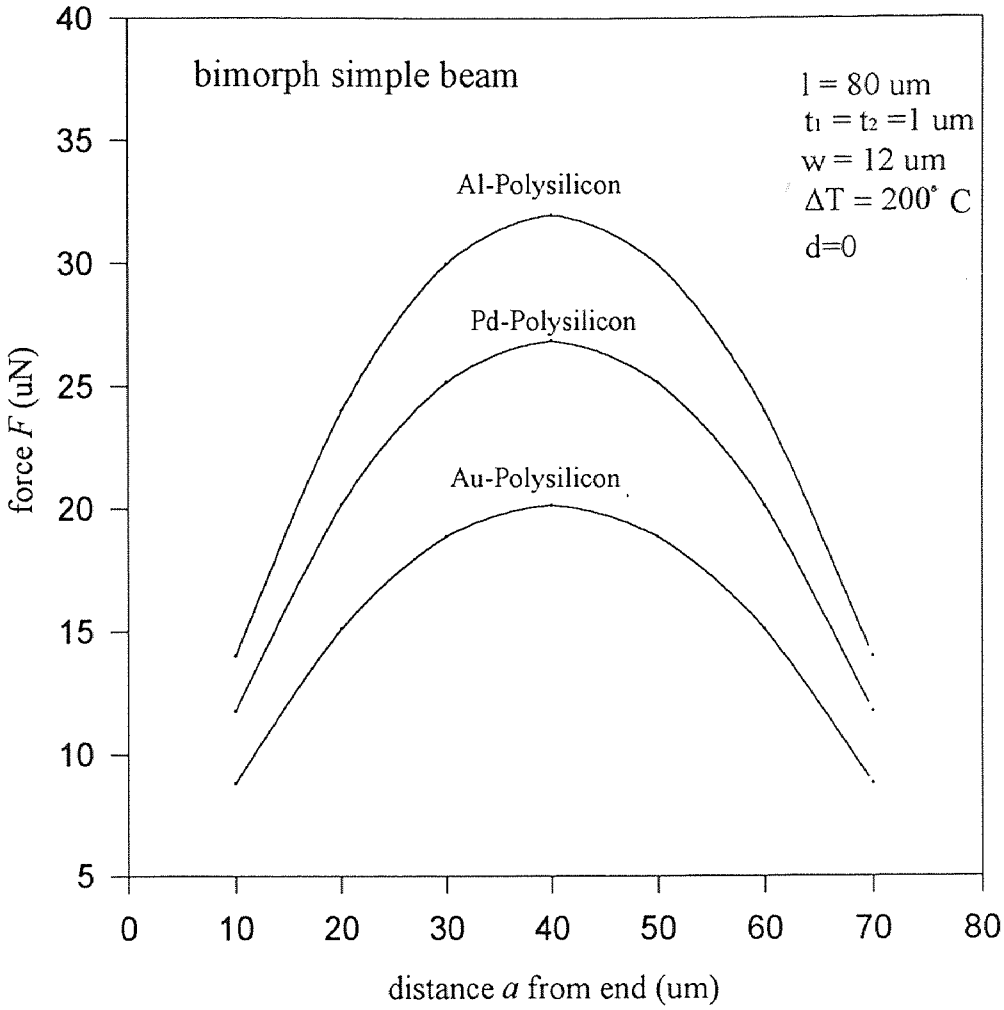

Figure 4.8 Force F versus distance a for different bimorph simple beams (ΔT=200°C)

4.3 Microactuator Structures for Programmable Antenna

The microactuators can be normally open(NO) or normally closed(NC) before it is excited. Various kinds of structures have been considered for this programmable antenna. Many factors such as dimensions, deflection, force , electrical contact and fabrication ease, must be taken into consideration. A simple beam structure has been chosen and detailed in Figure 4.9 and Figure 4.10. Other models are listed schematically in Appendix B.

Figure 4.9 shows a NO simple beam microactuator. It includes cross sections identifying materials and functions, respectively. This simple beam is built in a cavity between the gap along the antenna strip. Poly-Si and Pd(or Au) are combined together to form an sandwich structure. The Poly-Si is diffused with P and becomes n^+-poly. This n^+-poly is also the heater providing the thermal excitation to the beam when heated. The beam will deflect up and electrically contact the strip dipole conductor. The direction of deflection is up when heated since Pd(or Au) has greater thermal expansion coefficient than Poly-Si.

Between the Poly-Si and Pd(or Au) layers there is a very thin isolation layer Si_3N_4. The antenna strip is made of AI. The contact part is coated with gold. There is a structural material (Si_3N_4 or SO_2) on the top of the suspension part of the antenna strip. This can support the suspension part and also reduce the stress in the metal.

Figure 4.10 shows the top section view of the microactuator including the bonding pads and transmission line to the control circuit.

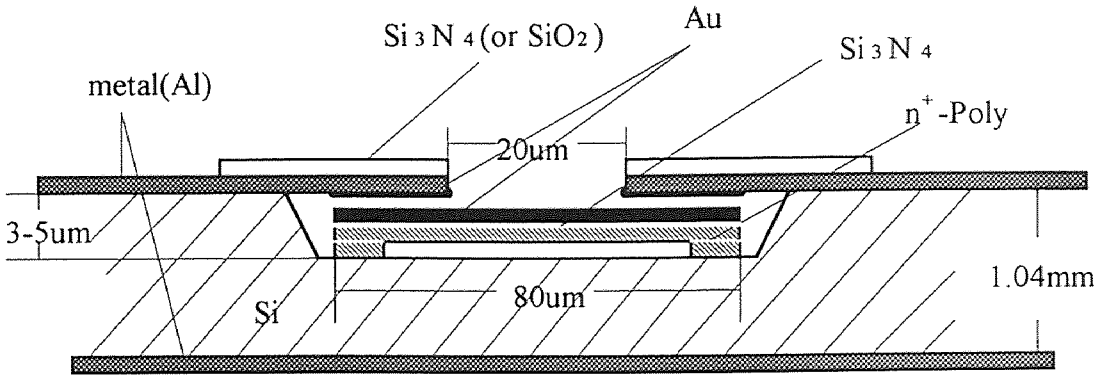

cross-section view identifying materials

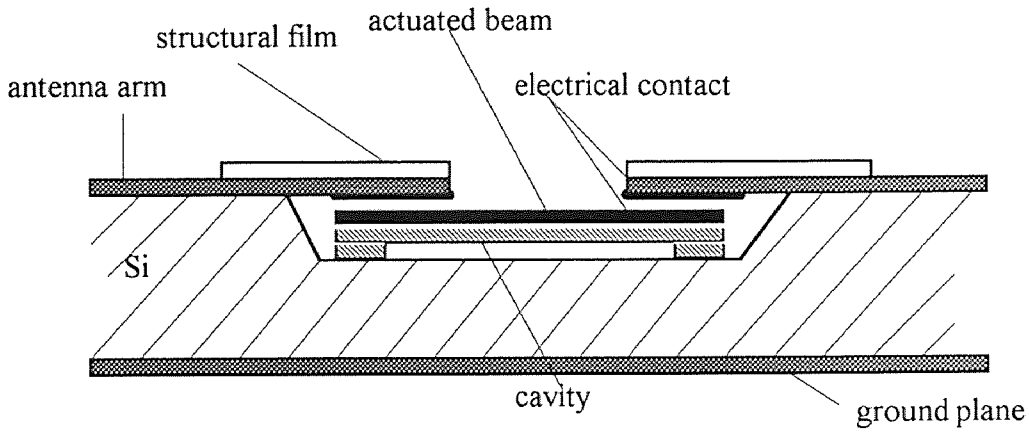

cross-section view identifying function

Figure 4.9 Cross-section views of microactuator for programmable antenna

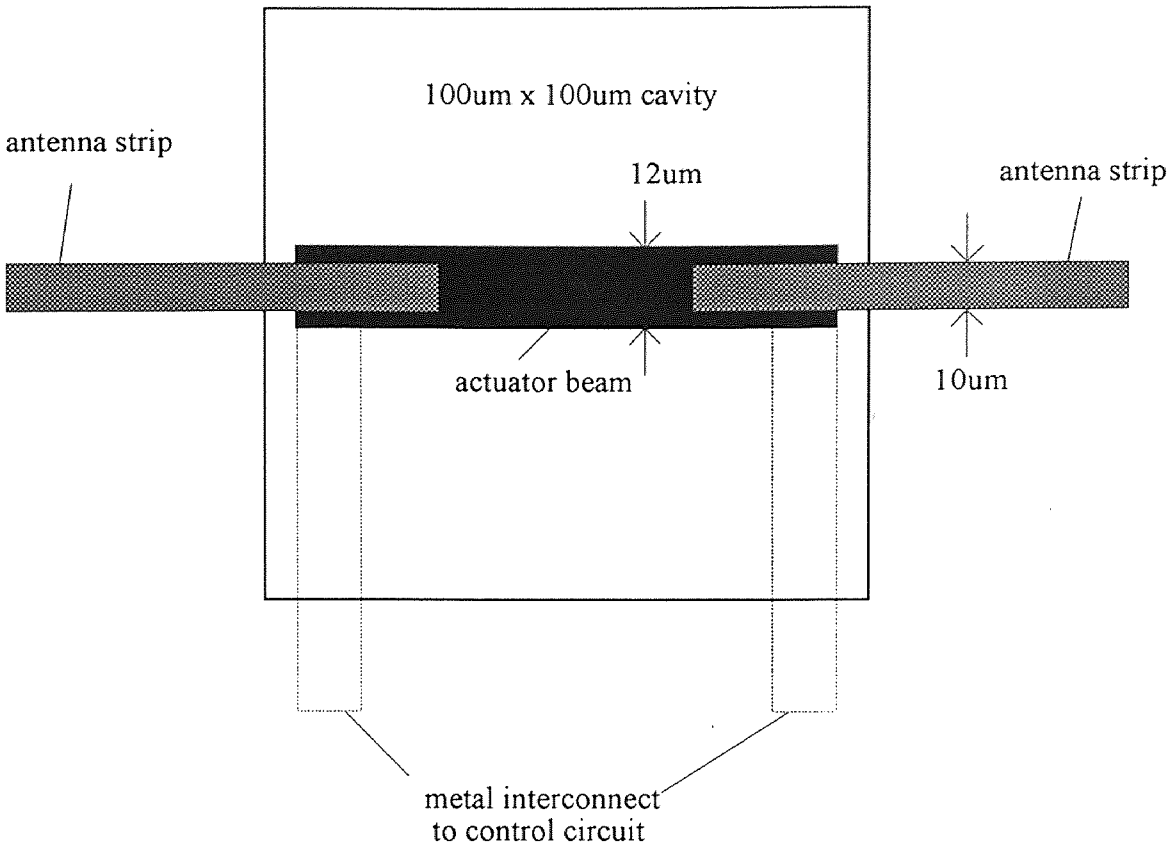

Figure 4.10 Top view of actuator beam with antenna strip and transmission line to control circuit

4.4 Mechanical and Electrical Considerations

The center deflections and forces have been discussed. The Au-polysilicon is chosen for the design. The design results and other related information are listed in Table 4.3.

Table 4.3 Data for the calculation of deflection d and force F with temperature rise ΔT

beam length l(μm)	80
width w(μm)	12
Poly-Si thickness t_2(μm)	1
metal-thickness(um) t_1(μm)	0.5
Poly-Si	
Young's modulus $E_2(10^{11}Pa)$	1.69
thermal coeff. of expansion $\alpha_2(10^{-6}/K)$	2.33
Au	
Young's modulus $E_1(10^{11}Pa)$	0.8
thermal coeff. of expansion $\alpha_1(10^{-6}/K)$	14.3
Pd	
Young's modulus $E_1(10^{11}N/m^2)$	1.67
thermal coeff. of expansion $\alpha_1(10^{-6}/K)$	13
force F (μN)	
at a distance *a*(in μm) from the fixed end	$0.00045(l-a)\,a\,\Delta T$
at a contact point distance $a = 30$ μm	$0.73\Delta T$
center deflection d (μm)	$0.196\,\Delta T^{1/2}$

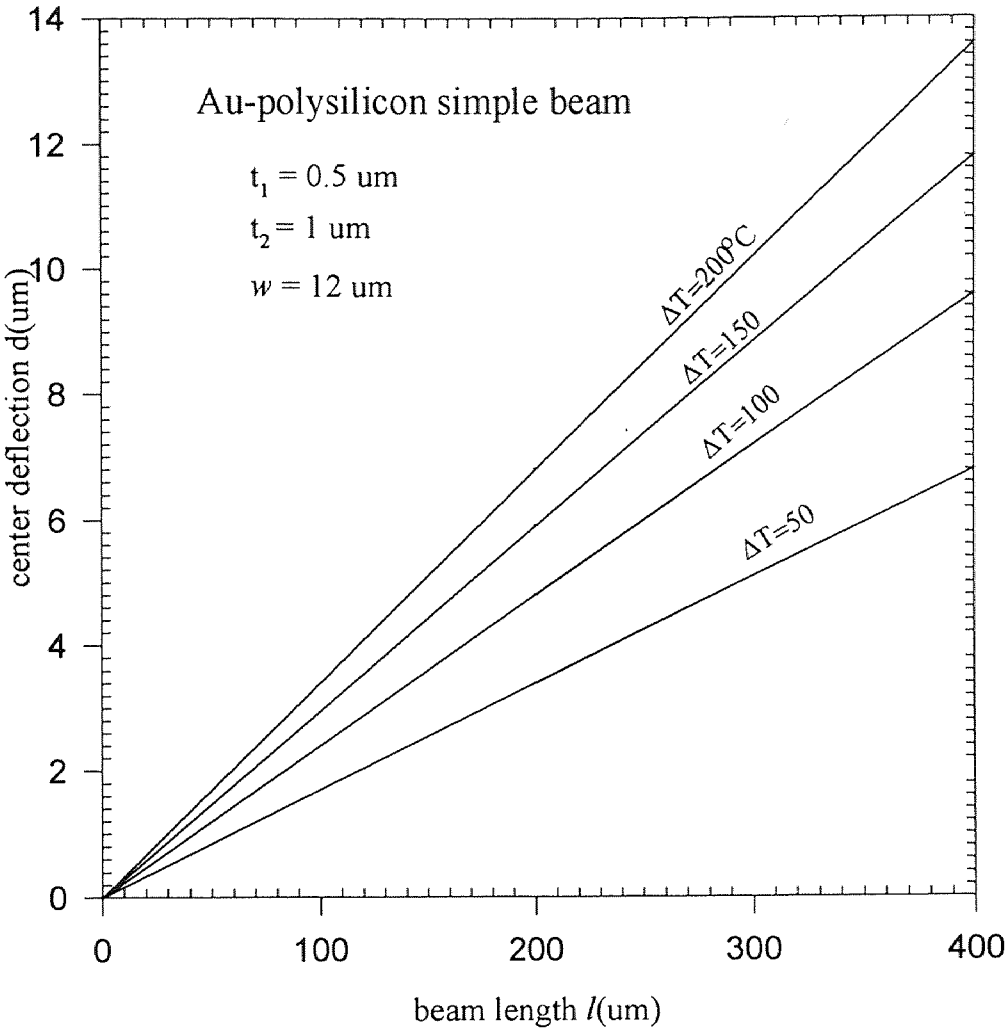

Figure 4.11 Center deflection d versus length l with different ΔT(°C) for a Au-Poly bimorph simple beam

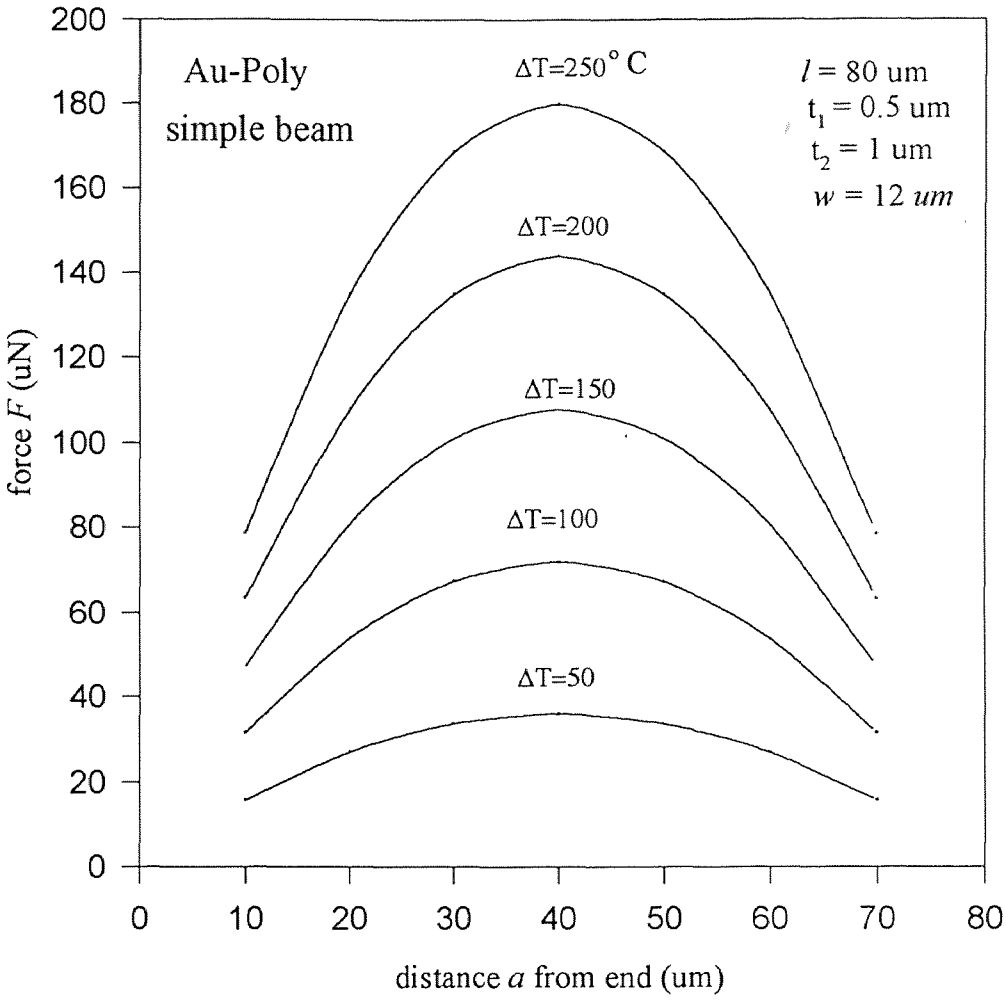

Figure 4.12 Force F versus distance a for a Au-polysilicon simple beam

There is a relationship between the force and the contact resistance. Experimental results have been reported by Hosaka[31] and a plot is shown in Figure 4.13. The average resistance decrease as the contact force increases and converges to about 2Ω. As shown in Figure 4.14, the contact force needed for stable resistance is lowest for Au. It is less than 100μN. As shown in Figure 4.15, open contact forces are limited to between 0-20μN. It is concluded that if gold is used as the contact material, the required contact forces is roughly 100μN. The contact-break force is roughly 0 N. The contact area is 20 μm^2.

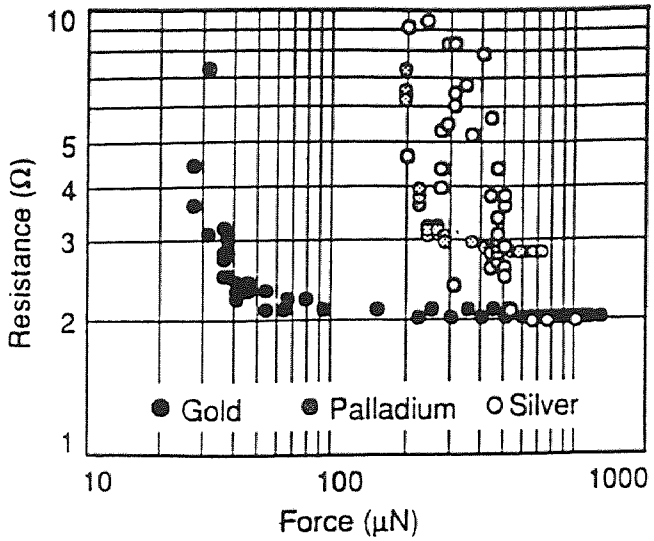

Figure 4.13 Relationship between on-resistance and contact force[31]

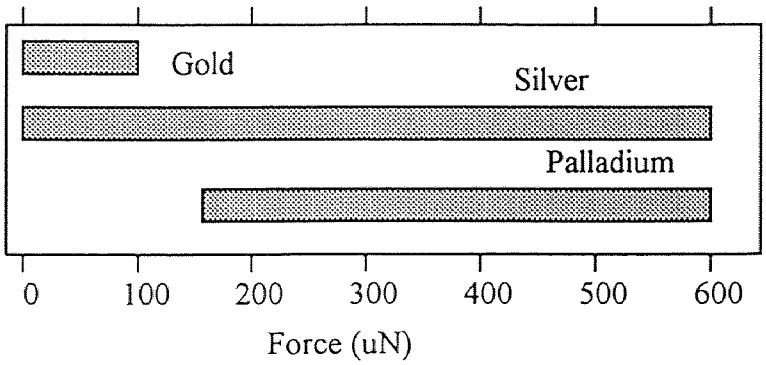

Figure 4.14 Contact force needed to establish stable resistance[31]

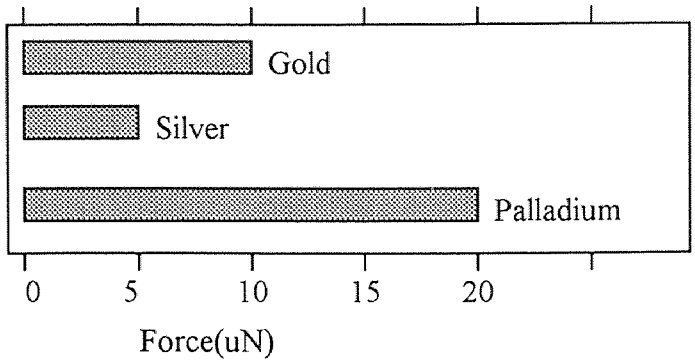

Figure 4.15 Maximum contact force for a completely open circuit contact[31]

Therefore according to the calculated result in Figure 4.12, a 200°C temperature rise is suitable for exciting the microactuator. The contact resistance is minimized to 2Ω. The center deflection d = 2.8um, which is obtained from Figure 4.10.

4.5 Heater Design

The microactuator is excited thermally. The n^+-poly layer is the heater and an external circuit provides the electrical current to the heater. The temperature along the beam is actually not uniform[32]. Figure 4.16 shows the temperature T along the length of a polysilicon beam. The doping concentration of the polysilicon is $1 \times 10^{19} cm^{-3}$. This doping concentration will be used in the processing later. Figure 4.16 is obtained when pressure $p = 1.3 \times 10^{-6}$Torr. The temperature rise will be greatly reduced under higher pressure, e.g., atmosphere pressure. Figure 4.16 can be a reference for the design. The estimated input current for the microactuator is at several mA current level. For example, 2 mA is required for a 250°C temperature rise.

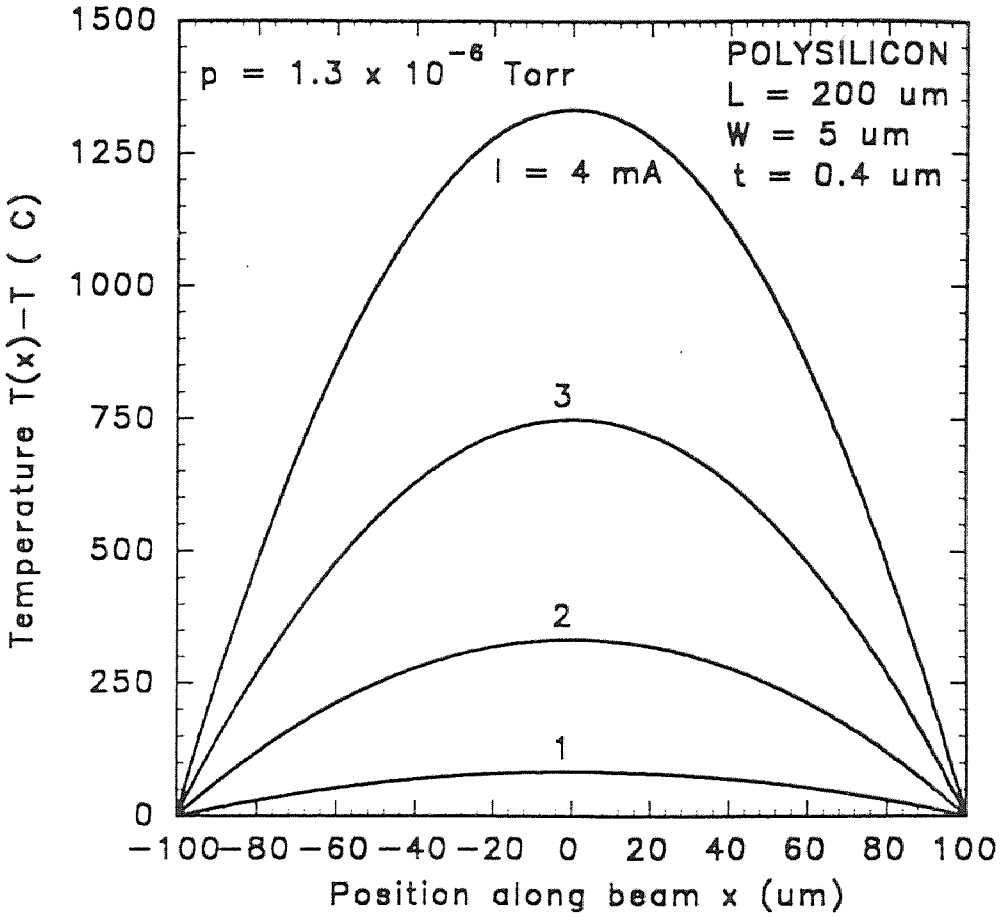

Figure 4.16 Variation of temperature along the length of the beam [32]

The needed input power p can be estimated.

$$p = I^2 R \tag{4.8}$$

where $R = \rho \frac{l}{wt} = \rho_{\square}(l/w)$.

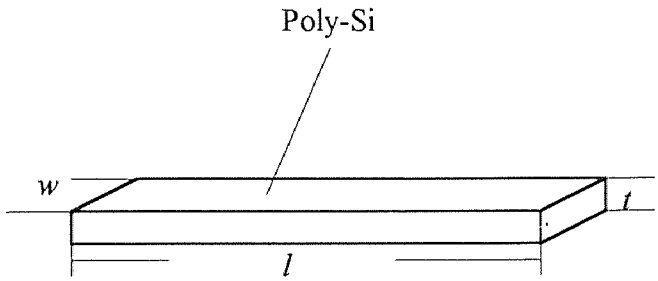

Figure 4.17 Geometry of polysilicon layer

The resistivity is determined by the doping concentration and the operating temperature[36]. If the hole concentration p is much greater than the electron concentration n as in p-type silicon,

$$\rho = \frac{1}{\sigma} \approx \frac{1}{q\mu_p p} \tag{4.9}$$

where

$$\mu_p \approx (m_p^*)^{-3/2} T^{1/2} \tag{4.10}$$

The temperature coefficient S_T can be presented as following based on (4.9) and (4.10):

$$S_T = \frac{1}{R}\left(\frac{\partial R}{\partial T}\right) = -\frac{1}{2T} \tag{4.11}$$

A n+-Poly with 1x 10^{19} cm^{-3} has a resistivity of about $\rho = 10^{-3}$ Ω·cm at room temperature[36].Then the resistance of the polysilicon layer with thickness t = 1 μm is about 10Ω/□ at room temperature. The temperature coefficient S_T = 0.17%/°C. The calculation results for the resistance and input power dissipation are tabulated in Table 4.4. The input power is usually in mili watts level.

Table 4.4 Estimation of power needed for the beam actuation (l=80μm, w= 12μm, t=1μm, S_T=0.17%/°C, ρ = 100Ω/□ at room temperature T=23°C)

ΔT(°C)	$\rho_{\square}$(Ω/□)	R = $\rho_{\square}$(l/w)(Ω)	I(mA)	P = I^2R(mw)
0	10	66.7	2.0	0.27
50	10.85	72.3	2.0	0.29
100	11.7	78.0	2.0	0.31
150	12.55	83.7	2.0	0.33
200	13.4	89.8	2.0	0.36
250	14.25	95.5	2.0	0.38
300	15.1	101.2	2.0	0.40

4.6 Processing Sequence

The processing sequence for fabricating a polysilicon simple beam and a cantilever beam are illustrated in Figure 4.18 and Figure 4.19 respectively.

As shown as in the Figure 4.19, an oxide layer is initially grown or deposited on the silicon wafer. The first masking step opens windows for the beam support areas, as shown in Figure 4.19(a). Polysilicon is then deposited by chemical vapor deposition (CVD), and pattered by reactive ion etching in the second masking step. An overlap of poly-Si is left around the perimeter of the oxide window to allow for misalignment error. If the poly-Si edge fails to overlap the oxide, then conventional RIE will erode the substrate after etching through the polysilicon layer. Next the wafer is etched in buffered HF to remove all oxide and release the poly-Si beam. In Figure 4.19(c) a free standing cantilever beam is created as illustrated.

A simple beam is made by including a second oxide window, as illustrated in Figure 4.18(a)-(d).

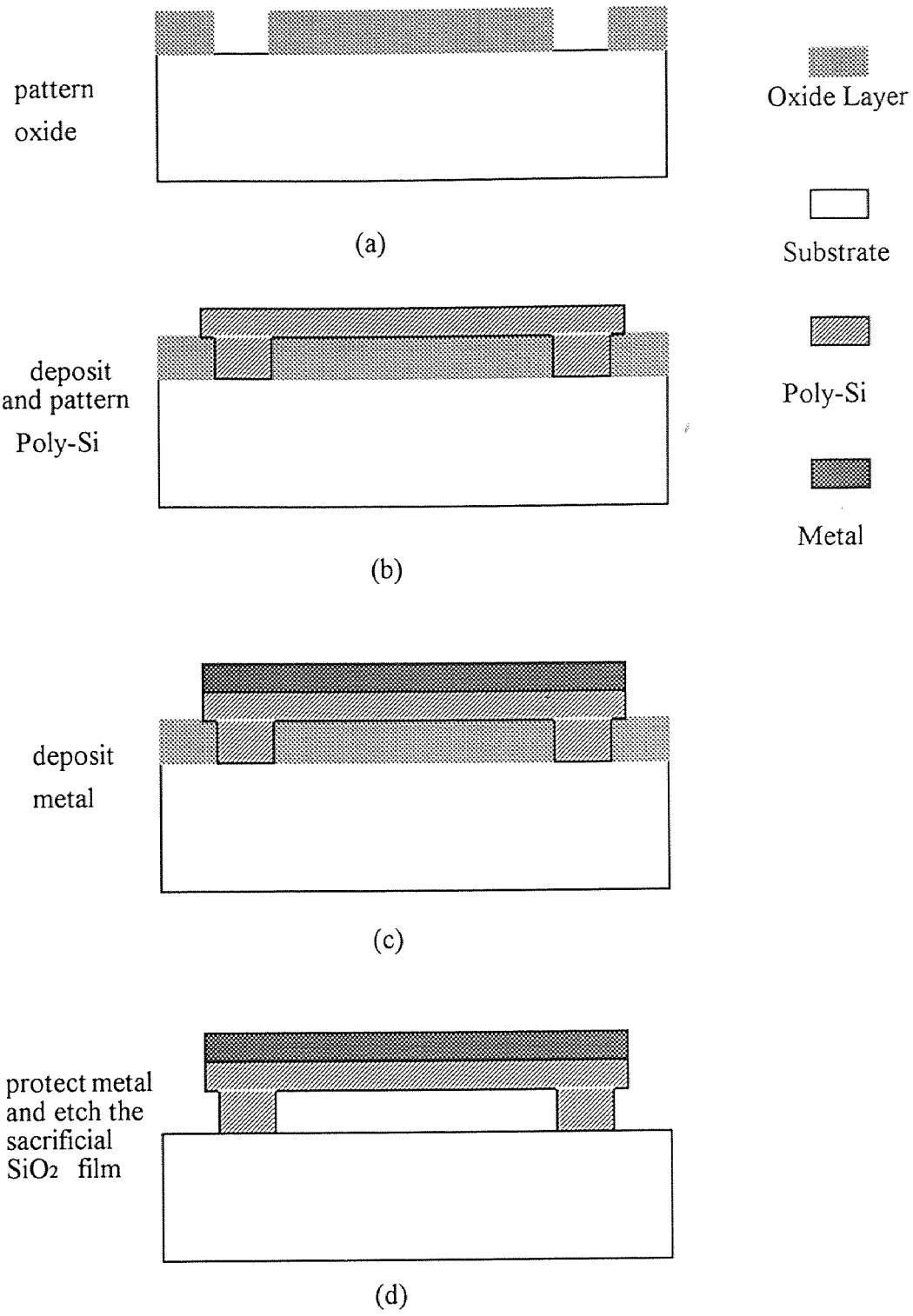

Figure 4.18 Processing sequence of a polysilicon simple beam

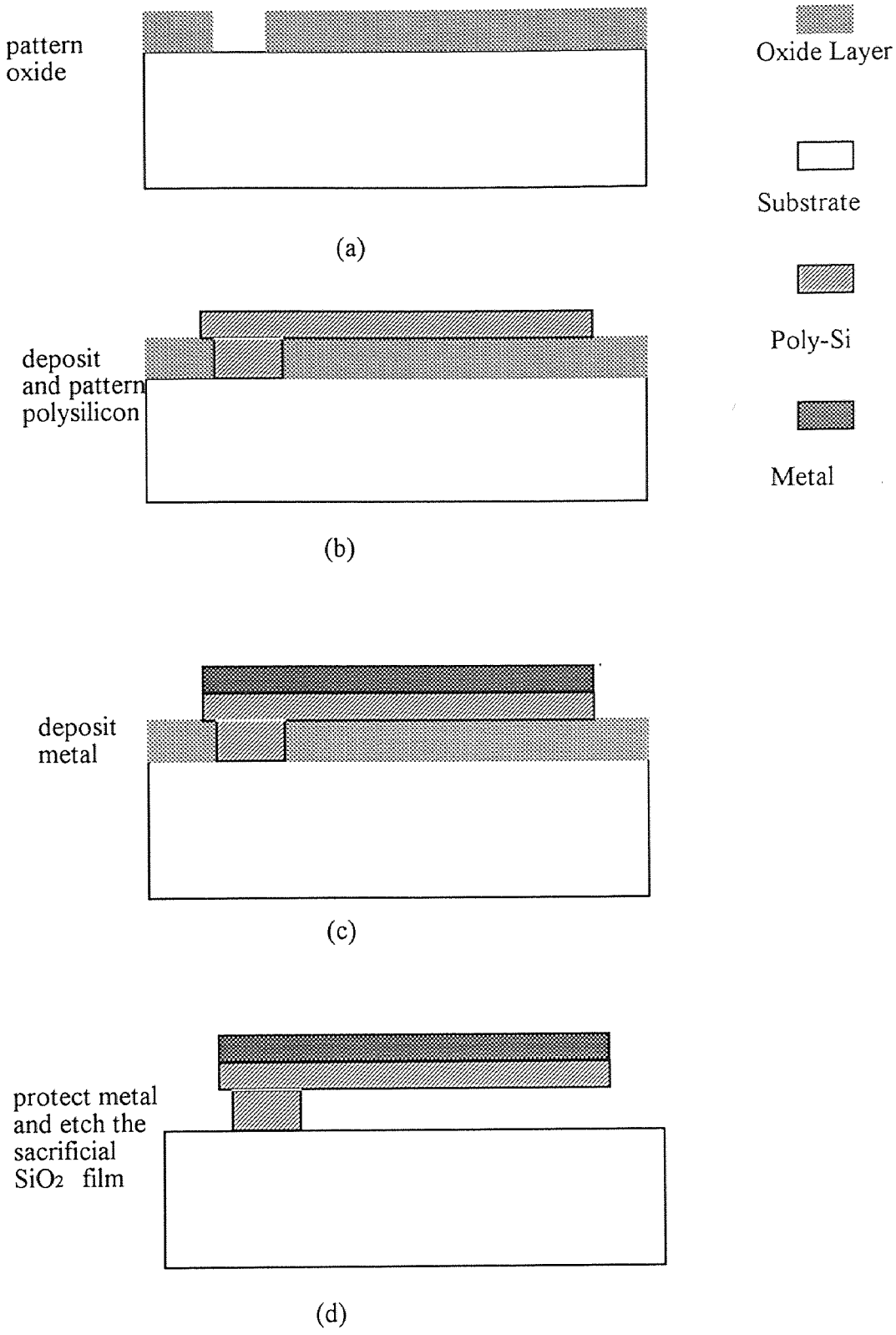

Figure 4.19 Processing sequence of a polysilicon cantilever beam

4.7 Conclusions for This Chapter

Microactuators can be designed to act as the microelectromechanical switches for the programmable antenna. Several factors must be taken into consideration for this design. These include:

1) enough deflection force to make good electrical contact

2) dimensions to be compatible with both micromachining and antenna

3) thermal heater to produce proper temperature profile

4) fabrication ease and compatibility with available semiconductor process technology.

Chapter 5

FABRICATION PROCEDURE

5.1 Processing Sequence

The processing procedure flow chart is shown in Figure 5.1-5.14. Only part of antenna strip and one microactuator are shown but it is enough for illustrating the fabrication procedure of this family of programmable antenna. The details of the fabrication procedure will be discussed in section 5.2.

The processing sequence of the programmable microstrip antenna can be summarized as following:

1. Starting material (P-type 100 Si)
2. RIE etching to open a well(cavity) (mask #1)
3. developing of LTO sacrificial layer and etching (mask #2)
4. depositing and patterning of Poly-Si layer (CVD) (mask #3)
5. doping of the Poly-Si layer via ion implantation
6. depositing and patterning of Si_3N_4 as isolation layer (mask #4
7. depositing and patterning metal(Pd) layer (sputtering) (mask #5)
8. spin-on glass as a sacrificial layer and Planerization
9. deposit thin film of Pd(contact surface) (mask #6)
10. depositing of Al as the antenna strip(metal sputtering) (mask #7)
11. deposit structural support layer (mask #8)
12. protect the device and metalize the back
13. etching of spin-on glass to release the structurehe

The above fabrication procedure is with respect to Figure 5.1-5.13. More detailed discussion will be presented with Figure 5.1-5.13 in next section.

5.2 Fabrication Procedure Description

1. Starting material

P-type silicon wafers oriented in the [100] crystallographic plane shown in Figure 5.1 are used in this thesis. This silicon wafer is with high resistivity(>100Ω cm).

First the silicon wafers are cleaned chemically to remove surface contamination. Aqueous mixtures of NH_4OH-H_2O_2, HCL-H_2O_2, and H_2SO_4-H_2O_2 are often used. These solutions are efficient in removing metallic impurities. The ammonium hydroxide and sulfuric acid based mixtures will also remove organic contaminants but the latter is better. These cleaning resolutions leave wafer surface in a hydrophilic state due to the oxidizing nature of the peroxide. In a hydrophilic state, water will wet the wafer surface since water can be retained by surface tension. The chemicals are removed by a short immersion in dilute hydrogen peroxide clean followed by the hydrofluoric acid since the chemically grown oxide can contain impurities from these chemicals. A typical cleaning sequence would be a sulfuric acid-hydrogen peroxide clean followed by the hydrofluoric acid dip, with deionized water rinses following each acid step.

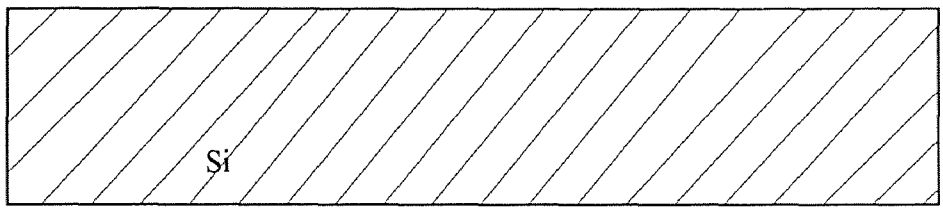

Figure 5.1 Starting material

2. Lithography (mask #1) and silicon substrate etch(RIE)

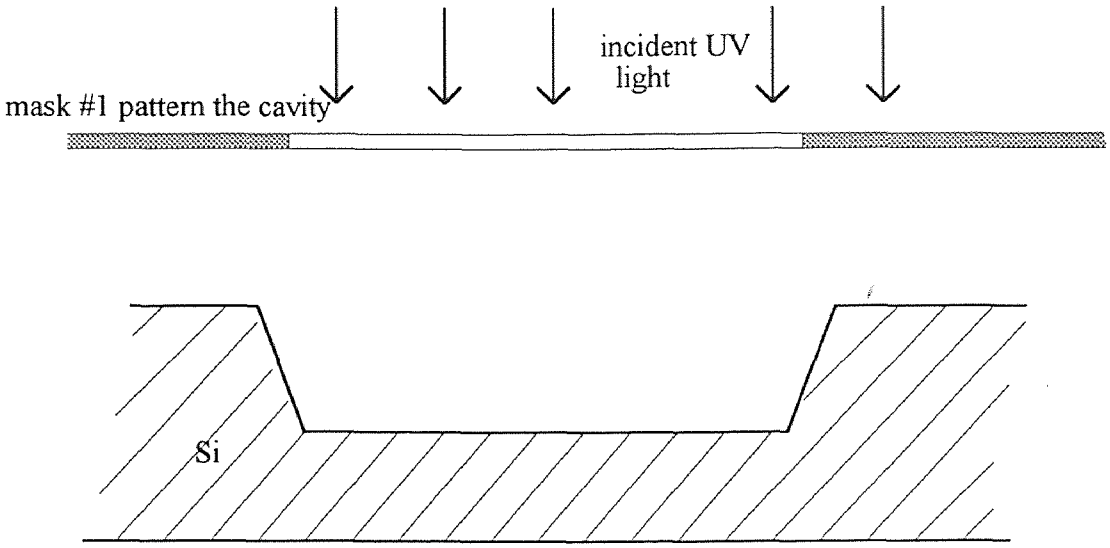

Figure 5.2 Pattern and RIE etch to open a flat-bottom cavity

The lithographic process is illustrated in Figure 5.2. The incident radiation is transmitted through the transparent parts of the lithography mask. The circuit pattern of opaque chromium blocks some of the radiation. This type of chromium/glass mask is used with ultraviolet (UV) light.

Optical lithography can be used to comprise the image with visible or ultraviolet radiation in a photoresist using contact printing. For integrated circuit production the line width limit of optical lithography lies near 0.4 μm although 0.2 μm features may eventually be printed under carefully controlled condition.

Either positive and negative resists can be used. Positive resists are used for this device. Positive resists contain two components: a resin and a photoactive compound dissolved in a solvent. The photoactive compound is a dissolution inhibitor. When it is destroyed by exposure to light, the resin becomes more soluble in an aqueous developer

solution, so higher resolution is possible with positive resists. The development process of projection printed images in positive resists has been modeled theoretical. It is an isotropic etching process. The sensitivity if most standard resists peaks in the 300 to 400 nm spectral range.

The window size the mask designs depends on the microactuator dimension. It is with area 100um x 100um and height 4 um in this design.

RIE(reactive ion etching is used to get this cavity. RIE has the following characteristics: physical, chemical, directional, and more selective than sputtering. The pressure of this etching is in the range of 100 millitorr.

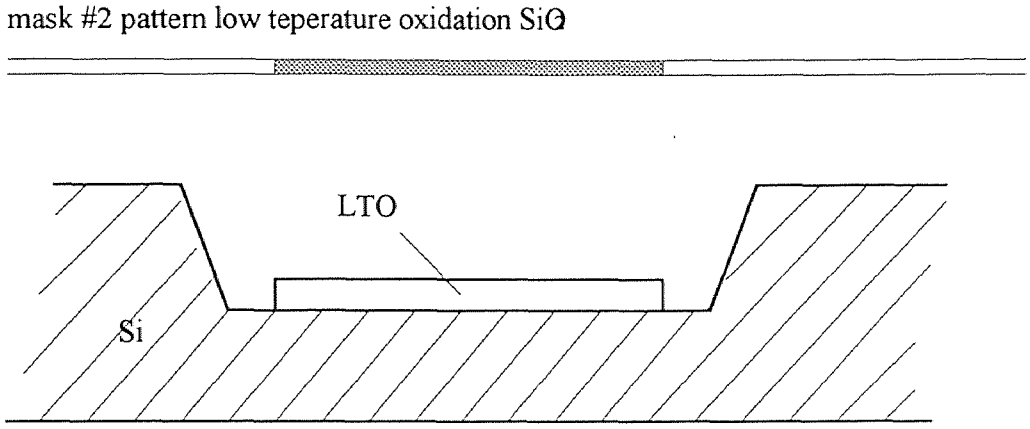

Figure 5.3 Deposit and pattern the LTO sacrificial layer

3. grow oxidation layer SiO_2 as a sacrificial layer

Several techniques to develop the oxide layers have been developed, such as thermal oxidation, et anodization, vapor-phase technique(CVD), and plasma anodization or oxidation. Since the SiO_2 layer is a sacrificial layer and a low-density is required, low temperature oxidation (LTO) is the preferred technique.

Then the oxidation layer is etched out patterned by mask #2 as shown in Figure 5.3.

4. Deposit Poly-Si followed by patterning

mask #3 define Poly-Si layer area

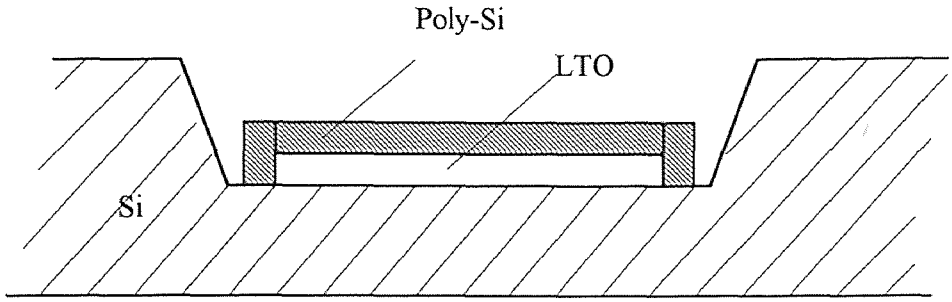

Figure 5.4 Deposit Poly-Si(CVD) layer

Poly-Si is prepared by pyrolyzing silane at 575 to 650°C. Polysilicon layer is deposited by LPCVD(Low temperature Chemical Vapor Deposition). The chemical reaction is

$$SiH_4 \rightarrow Si + 2H_2$$

The thickness of this Poly-Si layer is 1 um.

Wet etch is used to etch out the area which is not in the pattern. Polysilicon is typically wet etched in mixtures of nitric (HNO_3) and hydrofluoric aid (HF). The reaction is initiated by the HNO_3 which forms a layer of silicon dioxide on the silicon, and the HF dissolves the oxide away. The overall reaction is :

$$Si + HNO_3 \quad 6HF \rightarrow HSiF_6 + HNO_2 \quad +H_2 \quad +H_2O$$

Water can be used to dilute the etchant, but acetic acid (CH_3COOH) is preferred as a buffering agent, since it causes less dissolution of HNO_3 and thus yields a higher concentration of the undisipaciated species.

The mixture compositions can be varied to yield different etch rates. At high HF and low HNO_3 concentrations the etch is controlled by the HNO_3 concentration, because in such mixtures there is an excess of HF to dissolve the SiO_2 created during the reaction. n the other hand at low HF and high HNO_3 concentrations, the etch rate is limited by the ability of the HF to remove the SiO_2 as it is created. In such enchants the etching is isotropic, and they are used as polishing agents.

5. Dope via ion implantation

Doping concentration is $1x10^{18}$-$1x10^{19}cm^{-3}$.

6. deposit and pattern Si_3N_4 as isolation layer

This step needs mask #4. The thickness of the Si_3N_4 is 0.1μm.

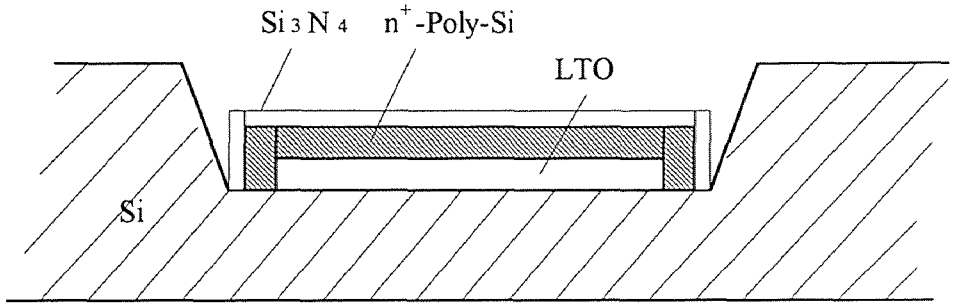

Figure 5.5 Deposit Si_3N_4 isolation layer

7. sputtering Pd and Pd removal

Sputtering is a mechanism in which atoms are dislodged from the surface of a materiel by collision with plasma-produced particles. It has become the most widely used deposition technique for a variety of metallic films in VLSI fabrication, including aluminum, aluminum alloy, platinum, gold, titanium: tungsten and tungsten.

Palladium(Pd) is utilized in the simple beam. Pd film is deposited with a thickness 0.5um. Wet etching can etch out Pd. This procedure is shown in Figure 5.6.

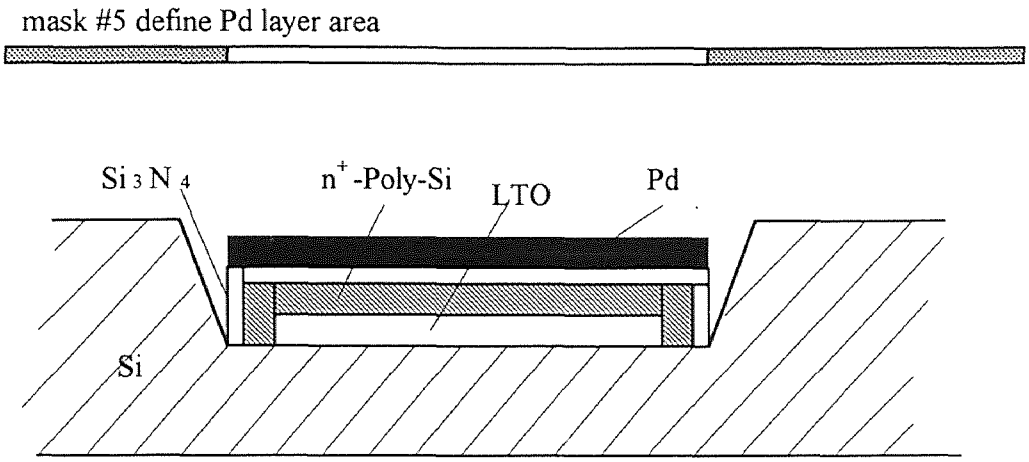

Figure 5.6 Deposit Pd layer

8. spin-on glass as a sacrificial layer and Planerize spin-on glass

The spin-on glass is liquid solutions to form doped SiO_2 layers. The spin-on dopants are applied to the wafers in a similar fashion as photoresist. The thickness of the deposit depends on the solution viscosity and the spin speed. The dopants concentration in the film can be varied by dilution with organic solvents. It is often necessary to bake the wafers at 200°C for 15 minutes to density the film, and to prevent absorption of water vapor prior to driving the dopant into the silicon. The diffusion is performed over a range of temperatures and times depending on the desired sheet resistance and junction depth.

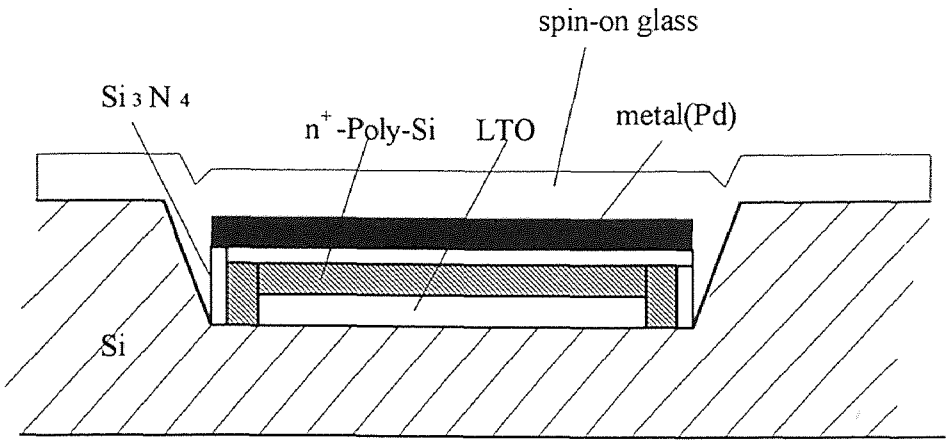

Figure 5.7 Spin-on glass as a sacrificial layer

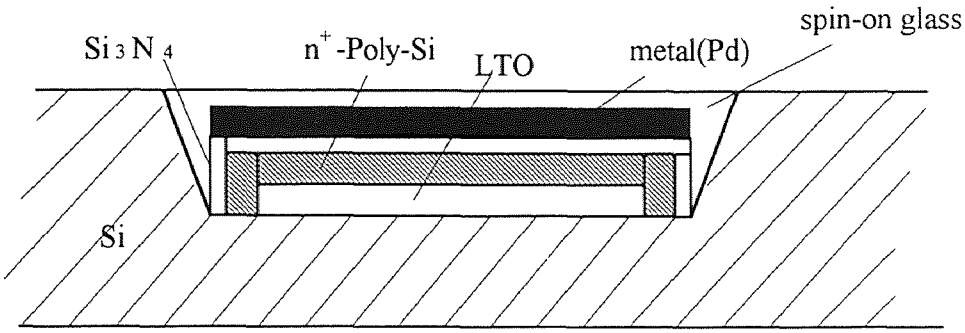

Figure 5.8 Planerize spin-on glass

The conformal deposition of a dielectric such as phosphorus-doped silicon dioxide over a pattern conduction layer results in a stepped profile. In order to insure a uniform coverage of the antenna strip the dielectric surface must be planerized. This can be accomplished by flowing the dielectric at high temperature (> 800°C). When the highest allowable substrate temperature is less than the dielectric flow temperature, two etching techniques can be used to smooth the surface. The first, called planerization, is

accomplished by spinning a resist or any other polymeric layer onto the irregular dielectric film, which is deposited thicker than necessary for the final structure. This results in a smooth of the new top surface. This new surface is then transferred to the dielectric by etching in a reactive plasma that etches the resist and the dielectric at the same rate. Smoothing of a dielectric surface can also be accomplished by depositing more dielectric than necessary and then etching in an RIE mode.

9. spin on metal Pd as contact area

mask #6 is required for the upper metal contact(sputtering Pd) as shown in Figure 5.9. Al is no good as a contact material because it always contains a thin oxide Al_2O_3 film insulator.

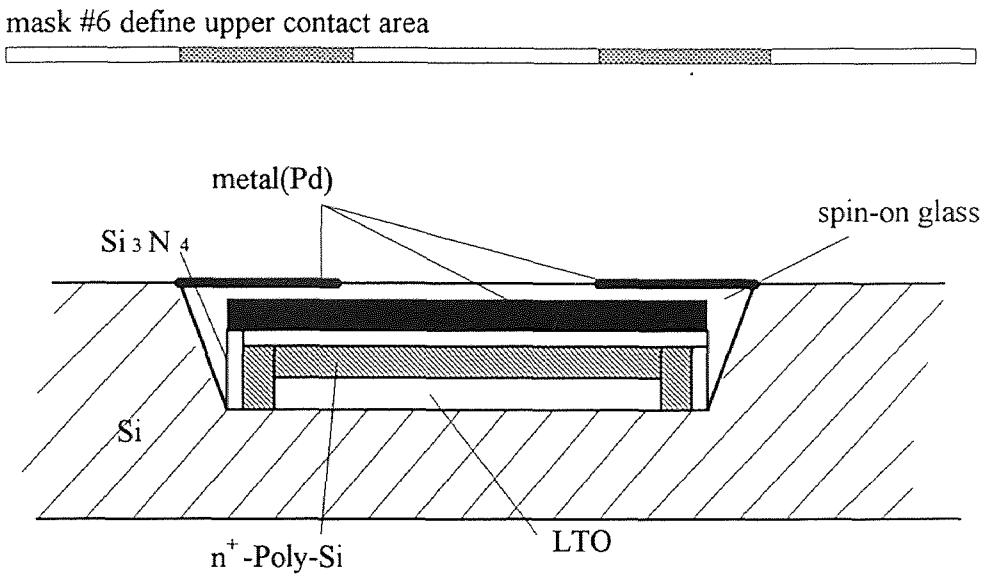

Figure 5.9 Sputtering and patterning upper metal contact

10. sputtering and patterning metal (Al) as antenna strip

Sputter metal Al with thickness of 0.2-0.5μm in this step. This metal layer forms antenna strip and feedline. mask # 7 is needed to define the area.

mask #7 define antenna strip and feedline

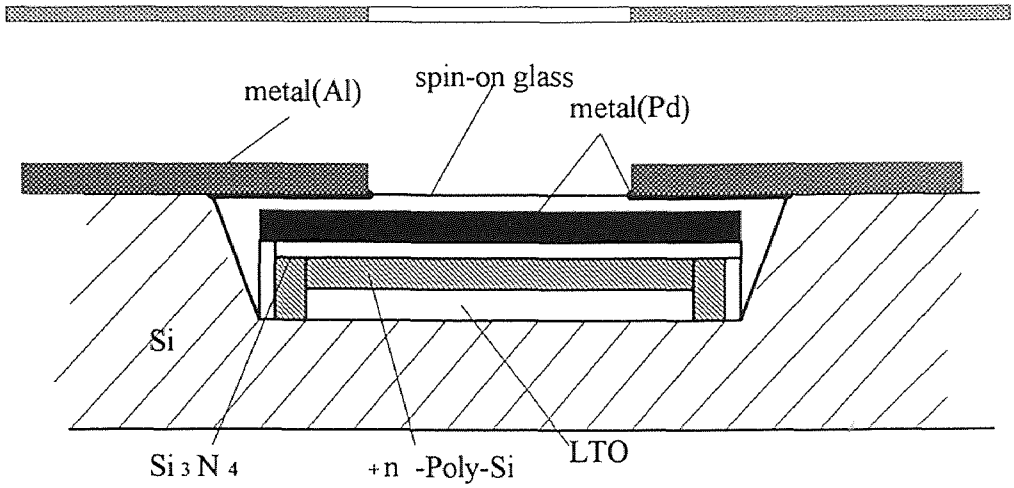

Figure 5.10 Pattern and develop antenna strip and feedline

11. deposit and pattern Si_3N_4 as a structural material

Same technique in step 4 will be used to form a structural layer.

mask #8 define structural material area

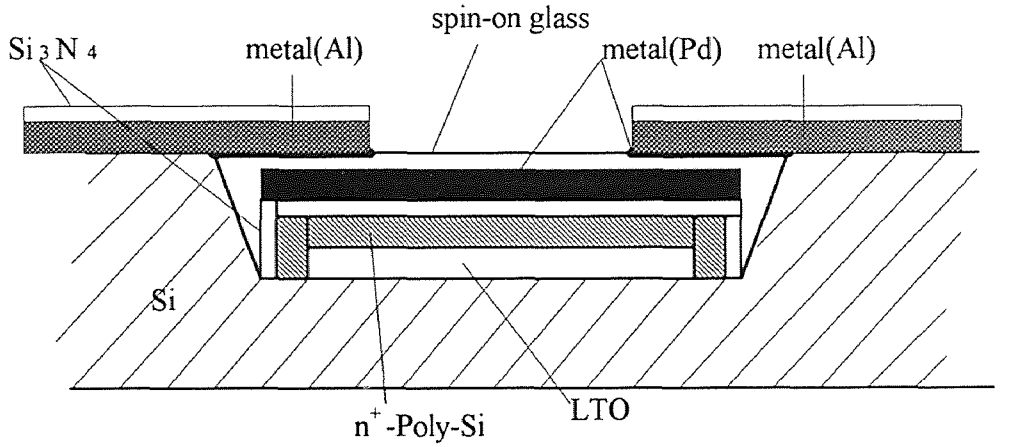

Figure 5.11 Deposit Si_3N_4 as structural material

12. back metalization

sputtering technique can be used to form a metal film on the back of the wafer while the device is protected. Mask is not needed.

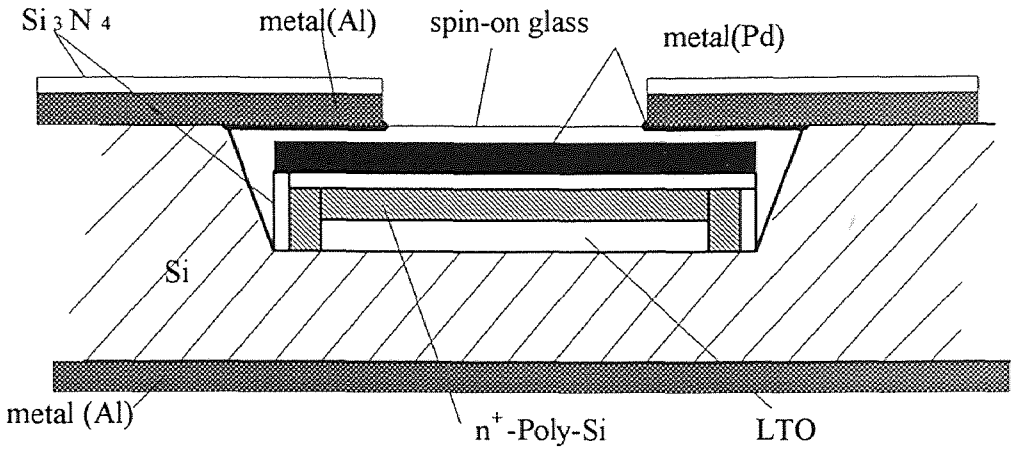

Figure 5.12 Metalize the back side

13. etch out sacrificial layers to release the structure

49% HF can be used to etch out the spin-on glass and LTO in the cavity. The etching rate depends on the density and doping of the spin-on glass and LTO. This speed is much faster than the etching rate of Al, Cu or Pd and Au. Therefore protection of the device is unnecessary.

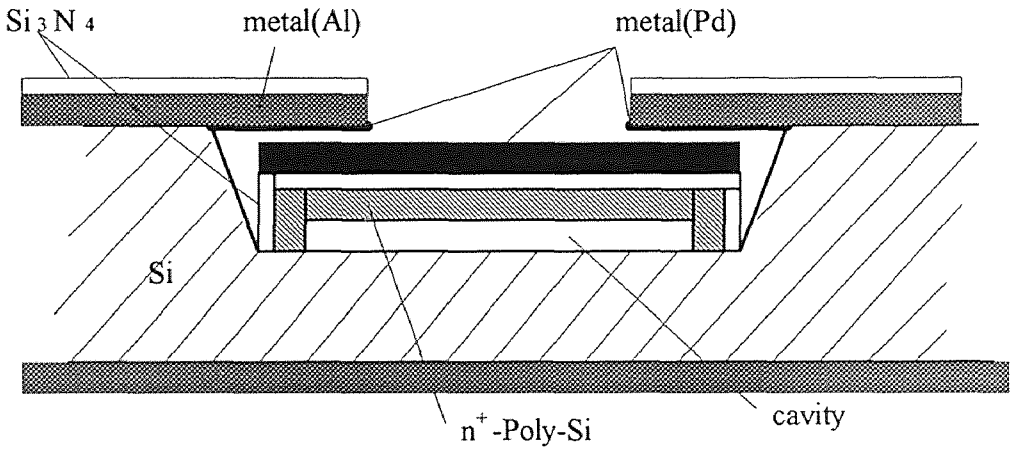

Figure 5.13 Etch out sacrificial LTO and glass layers

Chapter 6

CONCLUSIONS AND SUMMARY

The application of thermal actuators has resulted in a broad bandwidth programmable microstrip dipole antenna. The problem of narrow band width of microstrip dipole antenna can be solved by this proposal.

The theoretical analysis and simulations have been done on this innovative device. The research is focused on the input impedance of the antenna since it is a crucial parameter related to the antenna bandwidth. The radiation pattern and feedline also have been taken into consideration. The effective load capacitance because of the presence of microactuators is investigated in a simple model. This model is shown in Figure 2.5 in which the substrate is not included. The mechanism of thermal actuators is also discussed and several models for the programmable antennas are proposed. The following conclusion are drawn through the research:

1) the antenna working frequency can be tuned by changing the antenna length; microactuators can be utilized as electro mechanical micro switches;

2) microactuators can change the current distribution as well as the effective length when calculating input impedance;

3) but microactuators has negligible effects on the antenna radiation pattern since its small dimension.

4) the discontinuity on the antenna arms caused by the microactuators has negligible effects on the input impedance in a simple model . Its effect on an real programmable microstrip antenna is unknown.

A programmable antenna has been design with details. This design also includes the thermal actuator design. The processing flow in NJIT cleanroom is discussed in the later

part of the thesis. This fabrication procedure is compatible with that for the general IC circuit.

The future work will be done in some aspects. The models used in simulations are not precise enough. More detailed model is needed to be developed. This new model will include capacitance effect, fringing effect, etc.

APPENDIX A

MOMENT METHOD FOR CALCULATING THE CURRENT DISTRIBUTION ON PRINTED ANTENNA [11]

The current distribution is obtained by solving Pocklington's equation by moment methods. The Pocklington's equation for printed wires can be written in the form

$$E_x(x,z,h)=\int_{L_x} I(x')\left\{k^2\Pi_x+\frac{\partial^2\Pi_x}{\partial x^2}+\frac{\partial^2\Pi_z}{\partial x\partial z}\right\}dx' \tag{A-1}$$

where x is the direction the dipole is in. For our case

$$\Pi_x=\lim_{z\to h} 2K\int_0^\infty J_0(\lambda\rho)e^{-\mu(z-h)}\frac{\lambda\, d\lambda}{D_e(\lambda)} \tag{A-2}$$

and

$$\Pi_z=\lim_{z\to h} 2K(1-\varepsilon_r)\int_0^\infty J_1(\lambda\rho)e^{-\mu(z-h)}\frac{\lambda^2\Phi_x d\lambda}{D_e(\lambda)D_m(\lambda)} \tag{A-3}$$

in the equation above the following parameters need to be defined:

$$D_e(\lambda)=\mu+\mu_e\coth\mu_e h \tag{A-4}$$

$$D_m(\lambda)=\mu\varepsilon_r+\mu_e\tanh\mu_e h \tag{A-5}$$

where

$$\mu = \left[\lambda^2 - k^2\right]^{\frac{1}{2}}, \quad \mu_e = \left[\lambda^2 - \varepsilon_r k^2\right]^{\frac{1}{2}},$$

$$K = -\frac{j}{4\pi\varepsilon_0\omega}, \quad \rho = \left[(x-x')^2 + (y-y')^2\right]^{\frac{1}{2}}, \tag{A-6}$$

and $\Phi_x = \cos\phi$, while $\Phi_y = \sin\phi$.

Considering the printed wire along the x direction, since the wire is unloaded at the ends, the unknown antenna current distribution *I(x')* must satisfy the end boundary condition

$$I(-l) = I(l) = 0 \tag{A-7}$$

In order to solve (A-2) for the antenna current *I(x')*, the method of moments is used. Accordingly, the wire is divided into equal augments. As it is usually, the proper choice of current expansion function must be made. Sinusoidal expansion functions are still useful in this case for thin antennas for the advantages mentioned before in Section 2.4. The form of the ith expansion function centered at x_i is simply as follows, which is a little more complex than (2.3):

$$I(x') = \begin{cases} I_i\left[\dfrac{\sin k(d-\left|x'-x_i\right|)}{\sin kd}\right], & \left|x'-x_i\right| \le d \\ 0 & otherwise \end{cases} \tag{A-8}$$

where d is the length of each segment given by $d = 2l/N$.

Substitute the N-1 term current expansion series into (A-1)

$$E_x(x,y,h)$$

$$= \frac{k}{\sin kd} \sum_{i=2}^{N} I_x \{ \Pi_x \Big|_{x_{i-1}} + \Pi_x \Big|_{x_{i+1}} - 2\cos kd \Pi_x \Big|_{x_i} + 2\cos kd \Pi \Big|_{x_i} - \Pi \Big|_{x_{i-1}} - \Pi \Big|_{x_{i+1}}$$

$$+ k \left[\int_{x_{i-1}}^{x_i} \Pi dx' \sin k(x' - x_{i-1}) + \int_{x_i}^{x_{i+1}} \Pi dx' \sin k(x_{i+1} - x') \right] \}$$

(A-9)

where Π_x is given by (A-3) and

$$\Pi = 2(\varepsilon_r - 1) \lim_{z \to h} \int_0^{\infty} J_0(\lambda\rho) \cdot e^{-\mu(z-h)} \frac{\lambda\mu \, d\lambda}{D_e(\lambda) \cdot D_m(\lambda)} \tag{A-10}$$

with

$$\rho = \left[(x - x')^2 + y^2 \right]^{\frac{1}{2}} \tag{A-11}$$

Note that (A-8) does not involve derivatives of Π_x and Π_z . The derivatives yield improper integrals for $z = B$. Further more, the expression for E_x is in closed form, as it involves integrals which are convergent in nature.

Sinusoidal functions are chosen as testing functions and both sides of (A-9) are multiplied by the testing functions given by (A-8), with the subscript I replaced by j and the variable x' by x. the integration with respect to x reduces the problem to the matrix form

$$[V] = [I]\,[Z] \tag{A-12}$$

where I is related to the currents on the subsections and V to the electromagnetic excitation column. Depending upon the feeding point, the corresponding excitation voltage is set to unity in the excitation column.

The radiation pattern and impedance can be obtained once the current distribution $I(x')$ has been solved from (A-12).

APPENDIX B

MECHANISM OF CANTILEVER BEAM

Cantilever beam has the similar mechanism as simple beam. One of the basic values describing the behavior of cantilever beam is the conversion factor γ. Combining the deflection d at the free end of the cantilever with the temperature change ΔT

$$d = \gamma \cdot \Delta T \tag{B-1}$$

Assuming a uniform heat distribution within the cantilever, the conversion factor is given by[15]

$$\gamma = \frac{l^2}{2r\Delta T} \tag{B-2}$$

for l << r with the bending radius r and length l of the beam.

Geometry of a cantilever beam is shown in Figure B.1. The two materials forming the action beam are labeled as 1 and 2 respectively. Assume that both layers have the same length at the room temperature. The formula for the bending radius r or the curvature k had been derived by Riethmuller[4], and was modified by Chu[16] later. Chu's solution matches the experimental result better. Corresponding to Figure B.1, Chu's formula is[16]:

$$k = \frac{1}{r} = \frac{6b_1b_2E_1E_2t_1t_2(t_1+t_2)(\alpha_2-\alpha_1)\Delta T}{(b_1E_1t_1^{\,2})^2 + (b_2E_2t_2^{\,2})^2 + 2b_1b_2E_1E_2t_1t_2(2t_1^{\,2} + 3t_1t_2 + 2t_2^{\,2})} \tag{B-3}$$

where

E_i is Young's modules

α_i is the thermal coefficient of expansion,

t_i is the thickness of the layer, and

b_i is the width of the layer

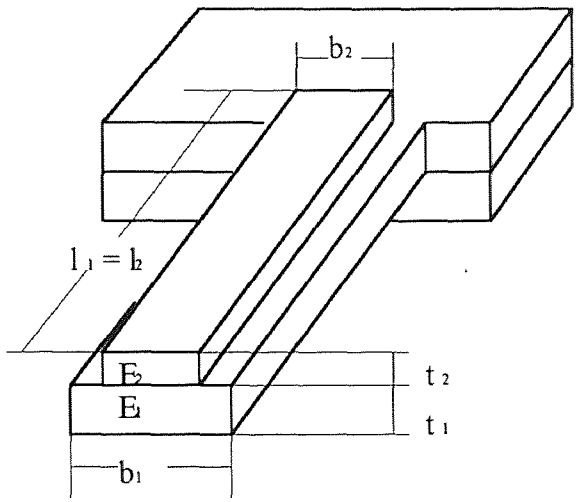

Figure B.1 Geometry of a typical bimetallic cantilever beam

If the different layers have identical geometry and dimensions and Young's modulus are similar in magnitude, the curvature k can be expressed as:

$$k = \frac{1}{r} = \frac{12(\alpha_2 - \alpha_1)\Delta T}{\left(\frac{m^2+1}{m} + 14\right) t} \tag{B-4}$$

where $m = \frac{E_1}{E_2}$.

The deflation d at the free end of the cantilever is a function of the constant curvature k introduced by thermal strain[16]

$$d = kL^2 / 2 \tag{B-5}$$

for L<< r.

The deflection d of the beam can also be expressed by a function of the electrical power P.

$$d = \gamma_e \cdot P \tag{B-6}$$

where $P = I^2 R$ with input current I and diffusion resistance R. γ_e is the effective conversion.

It is hard to derive a closed form for the effective conversion γ_e. γ_e is usually determined by experimental data.

Formula (B-5) is useful since it gives important rules to design thermal actuators: the absolute width of the structure does not affect the characteristics of the actuators. It is best if $\Delta\alpha$ and l are as large as possible and if t is as small as possible. Variations of Young's modulus have only a small effect on the conversion efficiency and can easily be compensated for by changing some dimensions of the second layer.

The length and the thickness are geometrical parameters and can be adjusted in a wide range. The values for $\Delta\alpha$ are limited by materials compatible with standard IC production steps and anisotropy etching techniques.

APPENDIX C

MICROACTUATOR STRUCTURES FOR PROGRAMMABLE ANTENNA

Figure C.1 shows a simple beam microactuator with NO actuation switches. Figure C.1 includes top view, cross section identifying materials and cross section identifying function. This simple beam is built on the gap along the antenna strip. Poly-Si and Au are combined together to form an sandwich structure. The beam will bend down and contact the strip when heated.

The structure in Figure C.1 is not strong enough unfortunately because of the stress of the metal. An improved device model is shown in Figure C.2. This is also a normally open simple beam structure. This simple beam structure has metal layer on the top of the polysilicon layer. The polysilicon layer supports the metal layer and reduces its stress. The beam will bend up to reach the stretching-out strips when heated.

The deflection of a simple beam is limited. Cantilever beam usually has more deflection than simple beam. A cantilever beam microactuator for programmable antenna is shown in Figure C.3. This improved model is based on the structure in Figure C.2. Similar to the simple beam in Figure C.2, the cantilever beam is also made of Au and Poly-Si with Au on the top of the Poly-Si. This cantilever beam is normally closed as shown in Figure C.3. The beam will bend down to make the antenna wire become open circuit when heated.

The simple beam structure in Figure C.4 is selected for the programmable antenna. For fabrication consideration it is better to fabricate the device in a cavity as shown as in Figure C.4. This design will avoid depositing thick Si_3N_4 layer as an isolation.

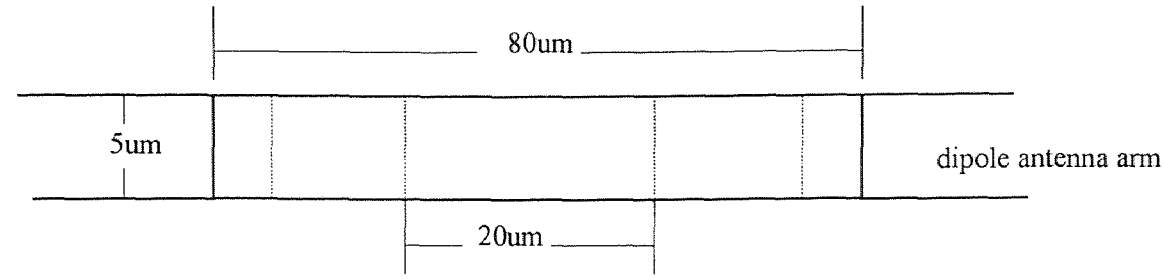

top view

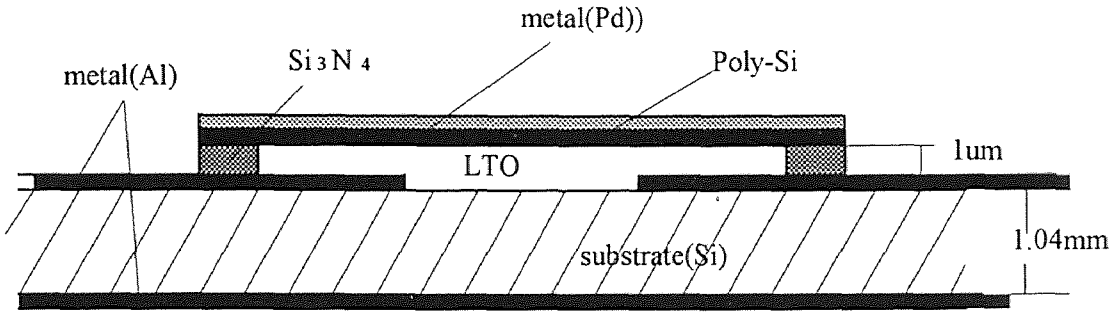

cross section identifying materials

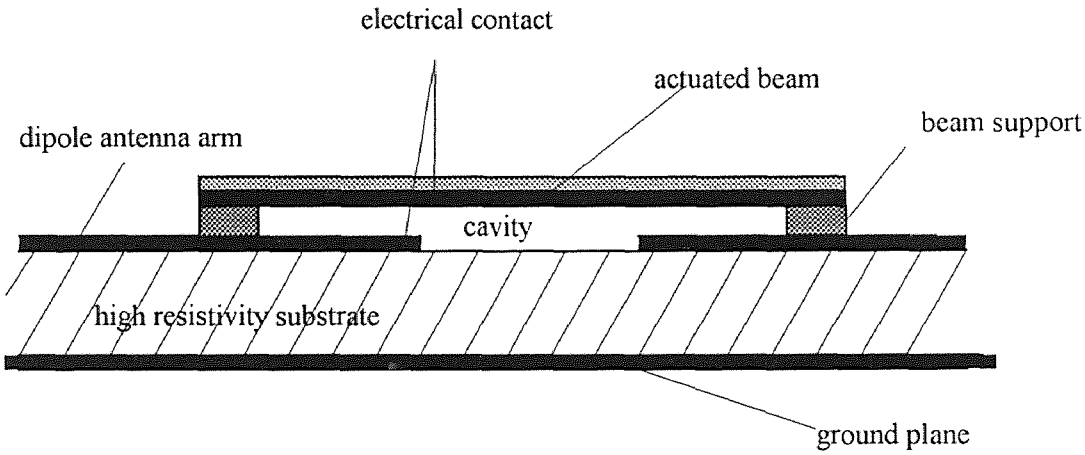

cross section identifying function

Figure C.1 Schematic views of a NO simple beam for programmable antenna

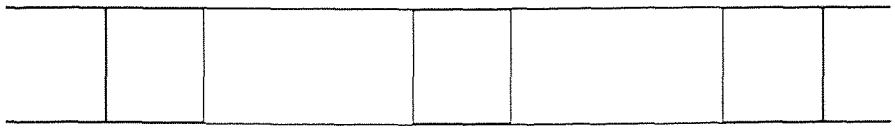

top view

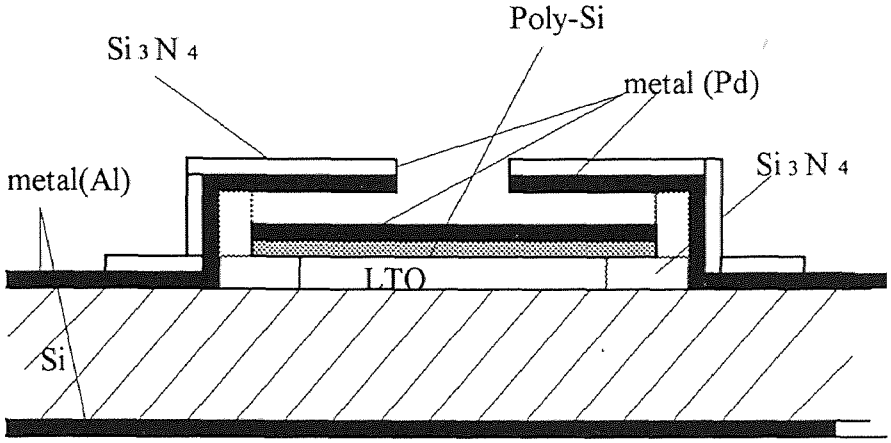

cross-section view identifying materials

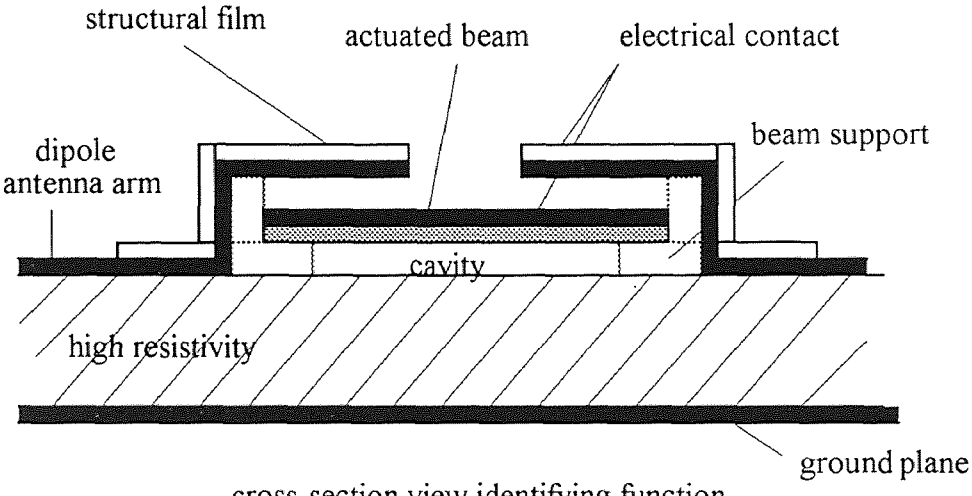

cross-section view identifying function

Figure C.2 Schematic views of a NO simple beam for programmable antenna

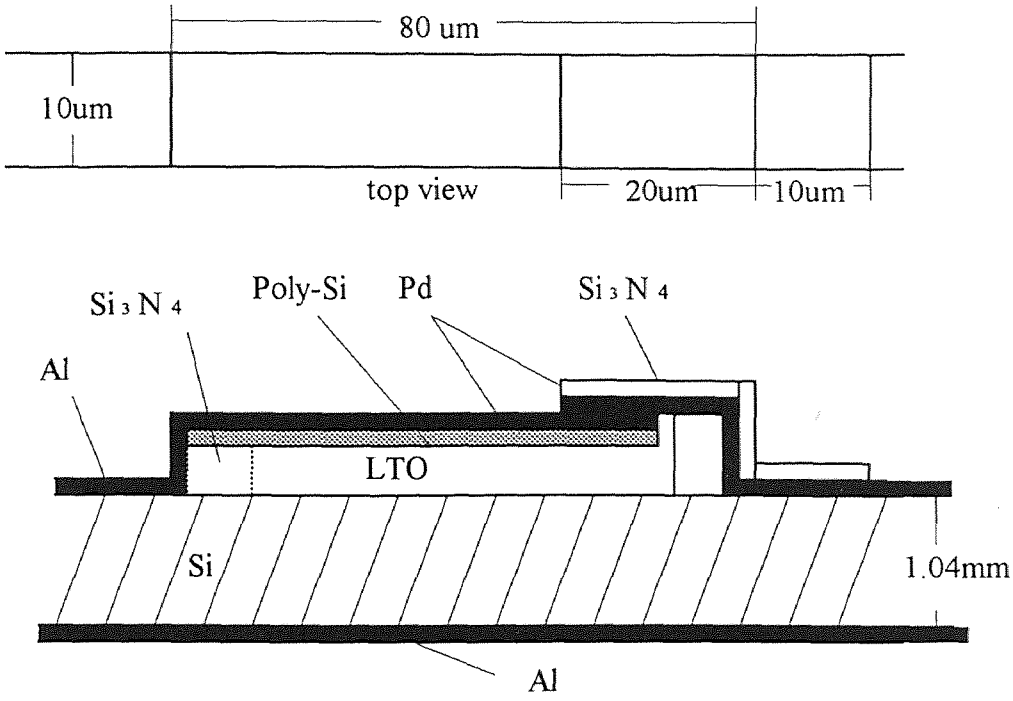

cross-section identifying material

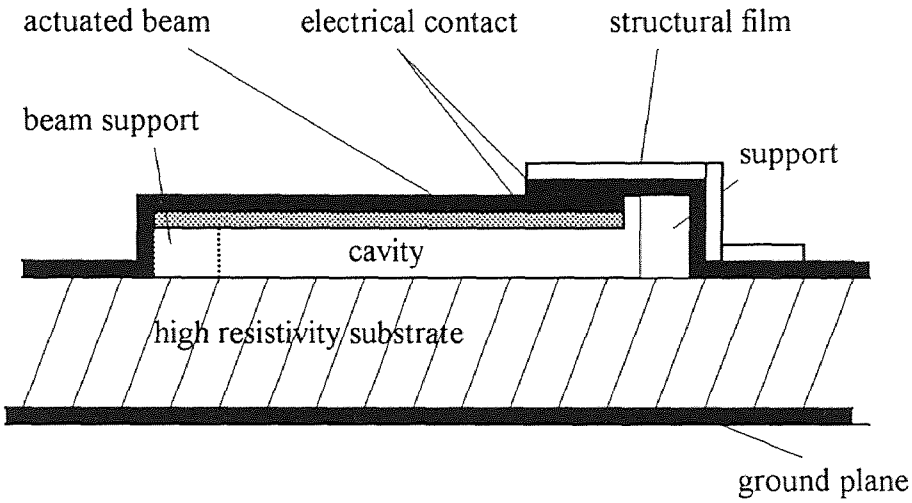

cross-section identifying function

Figure C.3 Schematic views of a cantilever beam for programmable antenna This structure can be NO or NC depending upon processing anneal and built in beam stress

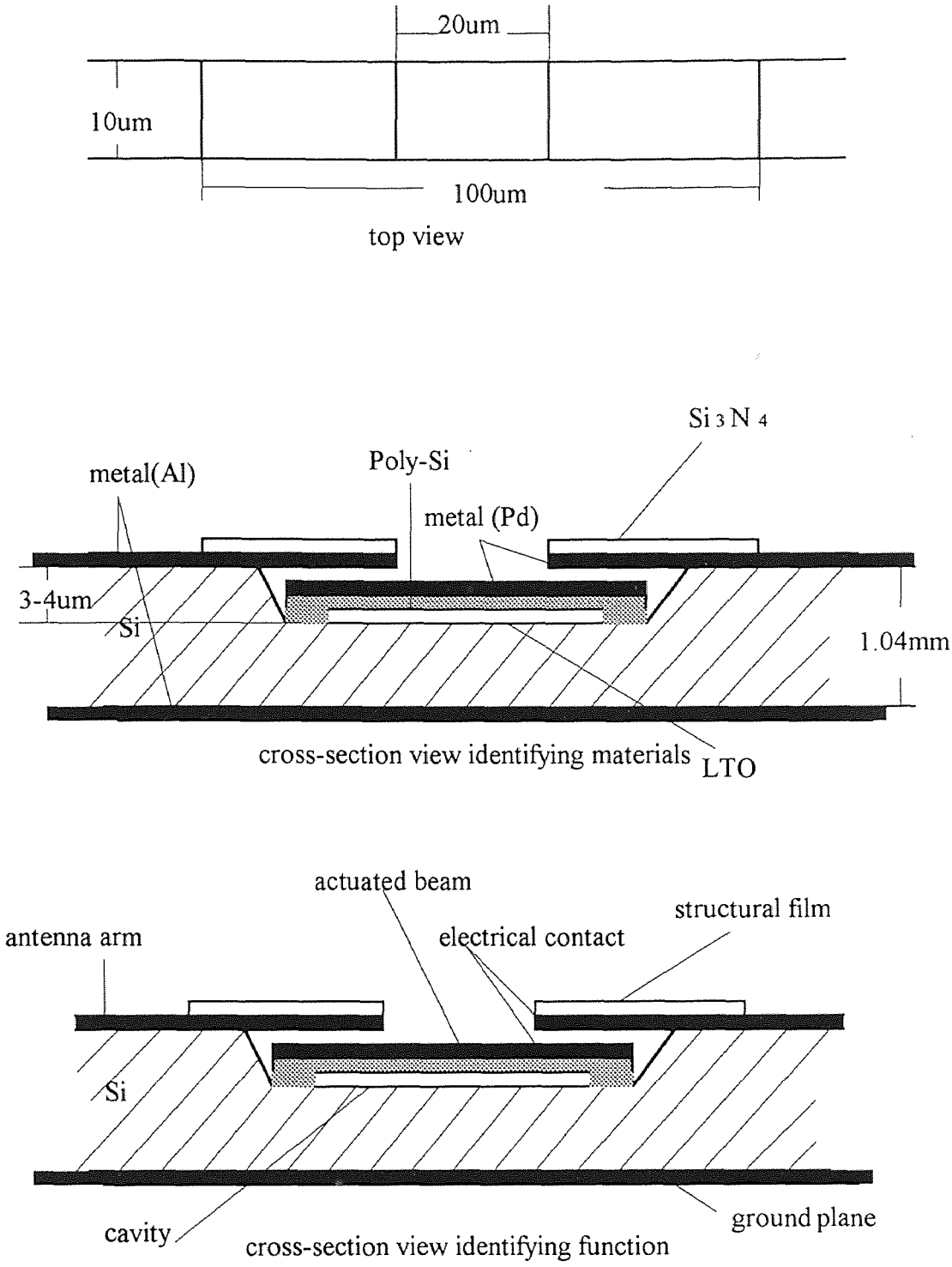

Figure C.4 Schematic views of a NO microactuator used for programmable antenna

APPENDIX D

DESCRIPTION OF I_NAC_3 AND SMAD

The highly portable I_NAC_3 software is developed by Compact Software, Inc, 483 mcLean Blvd, Paterson, NJ 07504. It has the following major output options and capabilities:

1) Far-field diagrams for all field components including magnitude and phase pattern, plots in polar or rectangular form, linear, lin-log or logarithmic scale, and gain over frequency.

2) Near-field distribution for all field components including 1,2,3 dimensional plots, plots in vector and contour form.

3) Current and charge distribution (only 1-dimensional, and all selected segment)

4) Impedance and loading including SMITH chart(for multiple sources), VSWR plots and peak load voltages and currents

5) Interactive rerun capability including new geometry, new incident field excitation and new frequency .

6) Time step plots including current, charge and near-field distributions.

7) Automatic disk file store and recall capability of input data, geometry data, current coefficients, impedances, far-field data, near-filed data, back-up and archive feature, and ASCII formatting for file interchange.

I_NAC_3 can only be used for the antennas in a uniform space with same dielectric constant. It can not be used for the simulation of microstrip antennas.

SMAD is used in the simulation for microstrip antenna. It is developed by Phraxos Research & Development Inc., Santa Monica, CA. It provides the following utilities which are not supported by I_NAC_3: current distributions, input impedance, and radiation patterns of microstrip antennas with rectangular and round shapes.

REFERENCES

[1] S. Timoshenko, "Analysis of bi-metal thermostats," J. Opt. Soc. Amer., Vol. 11, pp. 233, 1925.

[2] K. E. Petersen, "Silicon as a mechanical material," Proc. IEEE, Vol. 70, 1982, pp. 420.

[3] K. E. Petersen, " Micromechanical membrane switches on silicon," IBM J.Res. Develop., Vol. 23, pp. 376, 1979.

[4] W. Riethmuller and W. Benecke, "Thermal excited silicon microactuators," IEEE Trans. Electron Devices, Vol. 35, No. 6, June 1988, pp. 758-763.

[5] H. Matoba and T. Ishikawa, "A bistable snapping microactuator," Proceedings of IEEE Micro Electro Mechanical Systems, Oiso, Japan, Jan. 1994, pp. 45-50.

[6] N. Takeshima and H. Fujita, " Polyimide bimorph actuators for a ciliary motion system," (DSC-Vol. 32), ASME Winter Annual Meeting, Atlanta, GA, Dec. 1991, pp. 203-209.

[7] C. Liu, T. Tsao, Y. C. Tai, and C. M. Ho, " Surface micromachined magnetic actuators," Proc. IEEE Micro Electro Mechanical Systems Workshop, Oiso, Japan, Jan . 1994, pp. 57-62.

[8] E. Hashimoto, H. Tanaka, Y. Susuki, Y. Uenishi, and A. Watanabe, "Thermally controlled magnetization actuator (TCMA) using thermosensitive magnetic materials," Proc. IEEE Micro Electro Mechanical Systems Workshop, Oiso, Japan, Jan . 1994, pp. 108-113.

[9] B. Halg, "On a nonvolatile memory cell based on micro-electro-mechanics, " Proc. IEEE Micro Electro Mechanical Systems Workshop, Napa valley, CA, Feb. 1990, pp. 172-176.

[10] Y. Y. Lo, Antenna Handbook: *Theory, Applications, and Design* , New York, 1988 pp. 4.1-4.8 and pp. 10.9-10.27.

[11] I. E. Rana and Nicolaos G. Alexopoulos, "Current distribution and input impedance of printed dipoles," IEEE Transactions on AP, Vol. AP-29, No.1, Jan. 1981, pp. 99-105.

[12] B. Wagner and W. Benecke, "Microfabricated actuator with moving permanent magnet", Proceedings IEEE Micro Electro Mechanical Systems Workshop, Nara, Japan, PP. 27-32.

[13] C. H. Ahn, Y. J. Kim and M. G. Allen, "A planar variable reluctance magnetic micromotor with fully integrated stator and wrapped coils", Proceedings IEEE Micro Electro Mechanical Systems Workshop, Fort Lauderdale, FL, USA, Feb. 1993, pp. 1-6.

[14] S. Akamine, T. R. Albercht, M. J. Zdeblick, and C. F. Quate, " A planar process for microfabrication of STM," Proc. 5th Int. Conf. Solid-State Sensors and Actuators and Eurosensers III (Transducers '89), Vol. 2, Montreux, Switzerland, June 1989, pp. 243-246.

[15] W. Reithmuller and W. Benecke, "Thermally excited silicon microactuators," IEEE Transactions on Electron Devices, Vol. 35, No. 6, June 1988, pp. 758-763.

[16] W. H. Chu, M. Mehregany and R. L , "Analysis of tip deflection and force of a bimetallic cantilever microactuator," J. Micromech. Microeng. 3(1993) 4-7, pp. 4-7.

[17] S. P. Murarka, *Microelectronic Materials*, Academic Press, New York, 1989, pp.54.

[18] I. E. Rana, "Resonant length of linearly polarized microstrip radiator," Electronics Letters, Vol. 1, No. 18, 31st August 1978, pp. 594-599.

[19] J. M. Soares, S. B. De Assis Fonseca, and A. J. Giarola, " The effect of a dielectric cover on the current distribution and input impedance of printed dipoles", IEEE Transactions on AP-32, No. 11, Nov. 1984, pp. 1149-1153.

[20] C. A. Balanis, *Advanced Engineering Electromagnetics*, John Willey & Sons, New York, 1989, pp. 28-30.

[21] K. C. Gupta, R. Gary, and I. J. Bahl, *Microstrip Lines and Slotlines*, Artech House, Dedham, MA, 1979, pp. 45.

[22] L. T. Hwang, "A review of the skin effect as applied to thin film interconnections," IEEE Transactions on Components, Hybrids, and Manufacturing Technology, Vol. 15, No.1, Feb. 1992, pp. 43-54.

[23] B. Bustgens, W. Bacher, W. Menz, and W.K.Schomburg,"Micropump manufactured by thermoplastic molding," Proceedings. IEEE Micro Electro Mechanical Systems Workshop, Oiso, Japan, Jan. 1994.

[24] S. M. Sze, *VLSI Technology*, McGraw-Hill, New York, 1988, pp. 69.

[25] L. S. Fan, Y. C, Tai, and R. S. Muller, "IC processed electrostatic micromotors", Technical Digest, IEEE International Electron Devices Meeting, San Francisco, CA, Dec. 11-14, PP. 666-669, 1988.

[26] L. S. Fan, Y. C, Tai, and R. S. Muller, " IC processed micromotors: design, technology and testing", Technical Digest, 2nd IEEE Workshop on Micro Electromechanical Systems, Salt Lake City, Utah, Feb. 20-22, pp. 1-4, 1989.

[27] H. Guckel, T. Randazzo, and D.W. Burns, "A simple technique for the determination of mechanical strain in thin films with application to polysilicon," J. Appl. Phys., Vol. 57, no. 5, pp. 1671-1675, Mar. 1985.

[28] Y. J. Min, A. L. Palisoc, and C. C. Lee, "Transient thermal study of semiconductor devices," IEEE Trans. Components, Hybrids, and Manufacturing technology, 13, pp. 980-988, Dec. 1990.

[29] C. C. Lee and T. J. Su, "Transient thermal measurements using thermooptic and thermoelectric effects," IEEE 8th Annual Semiconductor Thermal Measurement & Management Symposium, 1992, pp. 42-46.

[30] R. J. Roark, W. C. Young, *Formulas for Stress and Strain,* McGraw Hill, Tokyo, Japan, 1976, pp. 108-113.

[31] H. Hosaka, H. Kuwano and K. Yanagisawa, " Electromagnetic microreleys: Concepts and fundamental characteristics," Proceedings. IEEE Micro Electro Mechanical Systems, Fort Lauderdale, Florida, Feb. 7-10, 1993.

[32] S. Talreja, "Microengineering thermal conducting vacuum pressure sensor", Master's Thesis, New Jersey Institute of Technology, 1990, pp. 58-59.

[33] S. P. Muraka, *Silicides for VLSI Applications*, Academic Press, New York, 1983, pp. 62.

[34] Y. Y. Wang, and T. L. kamins, *Poly-Si Film and its Application in VLSI*, Science Publisher, Beijing, P. R. China, 1988.

[35] D. K. Cheng, *Fields and Wave Electromagnetics*, Addison-Wesley, Reading, MA, 1989, pp. 80-93.

[36] S. M. Sze, *Physics of Semiconductor Device,* John Wiley & Sons, New York, 1969, pp. 39-43.